AGU PUBLICATIONS

JGR

Journal of Geophysical Research: Solid Earth

RESEARCH ARTICLE
10.1002/2014JB011768

Key Points:
- We constrain lake surface and level changes (1972–2011) of Siling Co in Tibet
- Multitemporal InSAR alllows to measure the subsidence due to lake load change
- Best fit rheological structure implies a ductile lower crustal channel

Supporting Information:
- Texts S1–S3 and Figures S1–S6

Correspondence to:
M.-P. Doin,
Marie-Pierre.Doin@ujf-grenoble.fr

Citation:
Doin, M.-P., C. Twardzik, G. Ducret, C. Lasserre, S. Guillaso, and S. Jianbao (2015), InSAR measurement of the deformation around Siling Co Lake: Inferences on the lower crust viscosity in Central Tibet, *J. Geophys. Res. Solid Earth*, *120*, 5290–5310, doi:10.1002/2014JB011768.

Received 15 NOV 2014
Accepted 4 JUN 2015
Accepted article online 8 JUN 2015
Published online 17 JUL 2015

InSAR measurement of the deformation around Siling Co Lake: Inferences on the lower crust viscosity in central Tibet

Marie-Pierre Doin[1], Cédric Twardzik[2], Gabriel Ducret[3], Cécile Lasserre[1], Stéphane Guillaso[4], and Sun Jianbao[5]

[1]University of Grenoble Alpes, CNRS, ISTerre, Grenoble, France, [2]Department of Earth Sciences, University of California, Santa Barbara, California, USA, [3]Laboratoire de Géologie, Ecole Normale Supérieure, Paris, France, [4]Computer Vision and Remote Sensing, Technische Universität Berlin, Berlin, Germany, [5]Institute of Geology, China Earthquake Administration, Beijing, China

Abstract The Siling Co Lake is the largest endorheic lake in Central Tibet. Altimetric measures, combined with lake contours, show that in 1972–1999 its water level remained stable, while it increased by about 1.0 m/yr in the period 2000–2006. The increased rate gradually stepped down to 0.2 m/yr in 2007–2011. The ground motion associated with the water load increase is studied by interferometric synthetic aperture radar (InSAR) using 107 ERS and Envisat SAR images during the period 1992–2011. The deformation amplitude closely follows the lake level temporal evolution, except that subsidence continues in 2008–2011, while the lake level stagnated. This temporal evolution suggests a non elastic relaxation process taking place at a decade timescale. Phase delay maps are used to constrain possible layered viscoelastic rheological models. An elastic model could partly explain the observed subsidence rate if elastic moduli are about twice lower than those extracted from V_P/V_S profiles. The surface deformation pattern is also extracted by projecting the phase delay maps against the best fit model temporal behavior. It shows that deep relaxation in the asthenosphere is negligible at the decade timescale and favors the existence of a ductile channel in the deep crust above a more rigid mantle. Overall, the best fit model includes a ductile lower crust, with a viscosity of $1-3 \times 10^{18}$ Pa s between 25 and 35 km and the Moho (at 65 km), overlying a rigid mantle.

1. Introduction

Constraints on the rheological properties of the crust and mantle are critical to the mechanical modeling of solid Earth deformation and of mountain belt formation. Laboratory experiments place bounds on the rheology; however, measurements in laboratory conditions must be extrapolated to natural setting. This extrapolation is particularly arguable for viscosity that depends strongly on temperature, strain rate, oxygen fugacity, hydration, melt fraction, etc..

"In situ" determination of the ductile mantle response to stress first came from global postglacial rebound studies, which constrain the lithosphere thickness, the upper mantle and top lower mantle viscosities. They lead to an elastic plate thickness of 80 to 120 km and an average mantle viscosity of about 10^{21} Pa s [*Peltier and Jiang*, 1996] possibly differentiated into a 4×10^{20} Pa s upper mantle and a 10^{22} Pa s lower mantle [*Lambeck et al.*, 1998]. However, global postglacial rebound studies are biased toward shield rheological structure, because large ice caps were mainly located on cratons [*Dixon et al.*, 2004; *Hyndman et al.*, 2005]. Rebound studies around smaller ice caps [e.g., *Lambeck et al.*, 1996; *James et al.*, 2009] or ancient lakes [*Nakiboglu and Lambeck*, 1983; *Bills et al.*, 1994a, 1994b, 2007] provide additional constraints on the local rheological structure of the uppermost mantle, showing that the uppermost mantle viscosity is lower away from shields than below them.

The mantle viscous behavior has also been inferred from postseismic deformation. The transient deformation following recent earthquakes shows that the lithosphere often deforms in response to slip events with timescales of the order of weeks to decades [*Cohen*, 1998; *Peltzer et al.*, 1998; *Piersanti*, 1999; *Pollitz et al.*, 2000; *Bürgmann and Dresen*, 2008]. This postseismic deformation, when interpreted in terms of crust or mantle ductile relaxation process, provides significantly lower estimates of the elastic thickness and of the viscosity in the lower crust and upper mantle than those derived from global postglacial rebound [*Satirapod et al.*, 2013; *Bürgmann and Dresen*, 2008; *Hammond et al.*, 2009]. However, in many cases the different mechanisms that

may explain postseismic deformation (afterslip, poroelasticity, and viscoelasticity) are difficult to distinguish using surface data [e.g., *Freed et al.*, 2006].

Geodetic measurement of the present-day surface deformation associated with recent surface loading can also provide constraints on the uppermost mantle rheology. Rebound studies associated with melting of ice caps in Iceland over the last hundred years [*Fleming et al.*, 2007] or Alaska [*Larsen et al.*, 2005] point toward a low-viscosity asthenosphere in these areas (a few 10^{18} Pa s). Such an approach can be extended to present-day lake load variations [*Kaufmann and Amelung*, 2000; *Cavalié et al.*, 2007], in order to constrain unambiguously the viscosity, where it is suspected to be particularly small (say, less than 10^{19} Pa s). It can also provide a lower bound on viscosity when the surface response to load is well explained by purely elastic models [*Nof et al.*, 2012]. However, this type of study is limited by the decade observation timescale and by the accuracy of modern geodetic techniques.

We present here a study of the deformation around the Siling Co Lake located in central Tibet using interferometric synthetic aperture radar (InSAR). The large lake size and large water level change provide a unique opportunity to probe the crust rheology in Central Tibet. Knowledge of the crust viscosity and elastic thickness in Tibet is crucial for our understanding of the orogen development. A very low viscosity in a continuous crustal channel should be able to accommodate large horizontal flux of crust material, equilibrating lateral variations in crustal thickness [*Royden et al.*, 1997; *Clark and Royden*, 2000; *Clark et al.*, 2005]. Crust viscosities lower than a few 10^{19} Pa s should also strongly alter the seismic cycle, leading to a prominent postseismic deformation and to discrepancies between short-term geodetic and long-term geologic locking depth and velocities across faults [*Trubienko et al.*, 2013; *Hilley et al.*, 2009; *He and Chéry*, 2008]. Finally, the presence of a viscous layer ($< 10^{22}$ Pa s) within the Tibetan crust reduces the effective long-term elastic thickness (7–20 km) and the support of relief over geologic timescales [*Masek et al.*, 1994; *Braitenberg et al.*, 2003; *Fielding and McKenzie*, 2012].

The paper is divided as follows. The first section describes the geological setting of Siling Co Lake. The next section focuses on the InSAR data processing and surface deformation measurement time. We then show the construction of the 1972–2012 lake load variations and the deformation model and discuss model sensitivity to the layered rheological structure. In the next section, we compare modeling results to data and invert for the best rheological structure beneath Siling Co, before discussing the result significance in the last section.

2. Lithospheric Structure of Tibet at Siling Co Location

The Siling Co in Tibet is a large endorheic lake in central Tibet of area ~2000 km^2, filling an E-W trending depression at 4500 m elevation (Figure 1). The elevation increases to 5000 m to the north and to the south. It is located against the Bangong Nujiang Suture (BNS) zone, within the Lhasa Block and south of the Qiangtang block. This area in central Tibet is marked by active E-W extension, with recent normal faulting seismicity on NS grabens [*Taylor and Yin*, 2009]. A salient feature to the south of the lake is the Pum Qu Xianza NS graben. The lake is in the middle of a conjugate strike slip fault system, right lateral and NW striking to the south (Gyaring Co) and left lateral and NE striking to the north, that can accommodate a few mm/yr of NS shortening [*Taylor and Peltzer*, 2006]. Numerous earthquake occurrences in the last 40 years shows that both normal and strike slip faults are active, although the amount of slip rate they accommodate is not really known. Block models integrating GPS data show that they possibly cumulate (adding the effect of a few normal and strike slip faults) up to a cm/yr displacement rate [*Loveless and Meade*, 2011].

The crustal structure at the location of Siling Co Lake is well constrained by the INDEPTH III profile, that extends further north the passive and active wide-angle seismic recordings of INDEPTH II experiment, going from the Lhasa block across the BNS zone into the Qiangtang block (Figure 1). It follows the northeast shore of the Siling Co Lake. Passive seismic recordings by this experiment in 1998–1999 shows numerous shallow earthquakes (depth less than 15 km) [*Langin et al.*, 2003]. The velocity structure includes a 5 km thick sedimentary layer, an upper crust down to 20 km, a middle crust to 35 km, and a thick lower crust down to Moho depth at 67 km [*Zhao et al.*, 2001; *Haines et al.*, 2003]. The BNS area is characterized by relatively low velocity in the top 30 km. No clear Moho step or sharp velocity contrasts in the crust are associated with the suture zone [*Zhao et al.*, 2001; *Haines et al.*, 2003]. The S velocity structure is depicted in *Mechie et al.* [2004], together with the Poisson ratio estimates (large in the middle and deep crust). No bright spots have been detected in the middle crust along the INDEPTH III profile, in contrast to southern Tibet [*Haines et al.*, 2003]. *Haines et al.* [2003] interpret these seismic evidences with either diffuse crustal fluid or dry but hot crust. Large but homogeneous

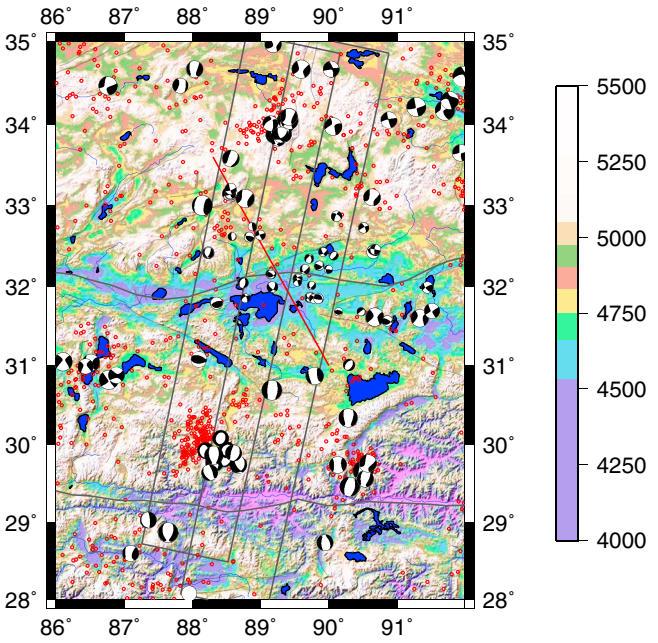

Figure 1. Location of the Siling Co Lake (31.7°N,89°E) superimposed on a color-shaded DEM map of central Tibet. Active faults (black lines) and the Indus and BNS suture zones (thick dark gray lines) are from *Taylor and Yin* [2009]. Focal mechanisms of earthquakes are from *Langin et al.* [2003] and from Harvard centroid moment tensor catalog from 1977 to 2009. Small red dots represent the earthquakes from the U.S. Geological Survey (USGS) catalog from 1973 to 2009. The dark gray rectangles display the limits of the ERS and Envisat tracks (overlapping descending tracks T219 and T491, from west to east) used for this study. The red straight line shows the approximate location of the Project INDEPTH (International Deep Profiling of Tibet and the Himalaya) Phase III (INDEPTH III) active seismic profile [*Haines et al.*, 2003].

attenuation observed along the INDEPTH III profile suggests abnormally high temperature and partial melt beneath the upper crust [*Xie et al.*, 2004]. *Mechie et al.* [2004] argue, from both the middle crust high conductivity anomaly and the seismic signal associated with the $\alpha - \beta$ quartz transition, that the 700°C isotherm is located at about 18 km depth beneath the BNS, deepening further south, resulting in partial melting in the middle crust.

Another wide-angle seismic reflection/refraction experiment that was conducted in the area is the 1982 Sino-French Tibet seismic program from Yaanduo to Siling Co [*Zhang and Klemperer*, 2005]. It shows a total sedimentary layer (low V_P, low V_S) approximately 8–10 km thick. A low-velocity zone appears at the base of the upper crust, at about 30 km. The middle crust then extends to 45 km, followed by a high-velocity lower crust down to the Moho at 65 km.

3. InSAR Data Processing

3.1. Data Set and Formation of Wrapped Interferograms

The SAR data set used in this study consists, on track T219, of 31 ERS images (from June 1992 to February 2011) and of 23 ENVISAT images (from April 2003 to August 2010), and, on Track T491, of 31 ERS images (from August 1992 to January 2011) and of 23 ENVISAT images (from December 2003 to September 2010) (Figure 2). Seven (nine, respectively) ERS images acquired after 2001 on track T219 (T491, respectively) have doppler centroid relatively consistent with earlier acquisitions. Processing these images offers the opportunity to link ERS and Envisat data sets into a continuous 1992–2011 time series. They allow us to monitor the deformation associated with the whole period of rapid lake level rise (2000–2010).

The New Small BAseline Subset chain described in *Doin et al.* [2011], from raw SAR images to coregistered differential interferograms in radar geometry, is applied to each acquisition geometry separately. We choose to compute highly redundant networks of "small" baseline interferograms (Figure 2). Large baseline (perpendicular baseline reaching 500 m or temporal baseline reaching 17 years) interferograms are also added when possible to (i) link all data on a given acquisition geometry, (ii) check interferogram consistency, and (iii) visualize large temporal baseline interferograms. We thus compute 106 (133, respectively) Envisat interferograms

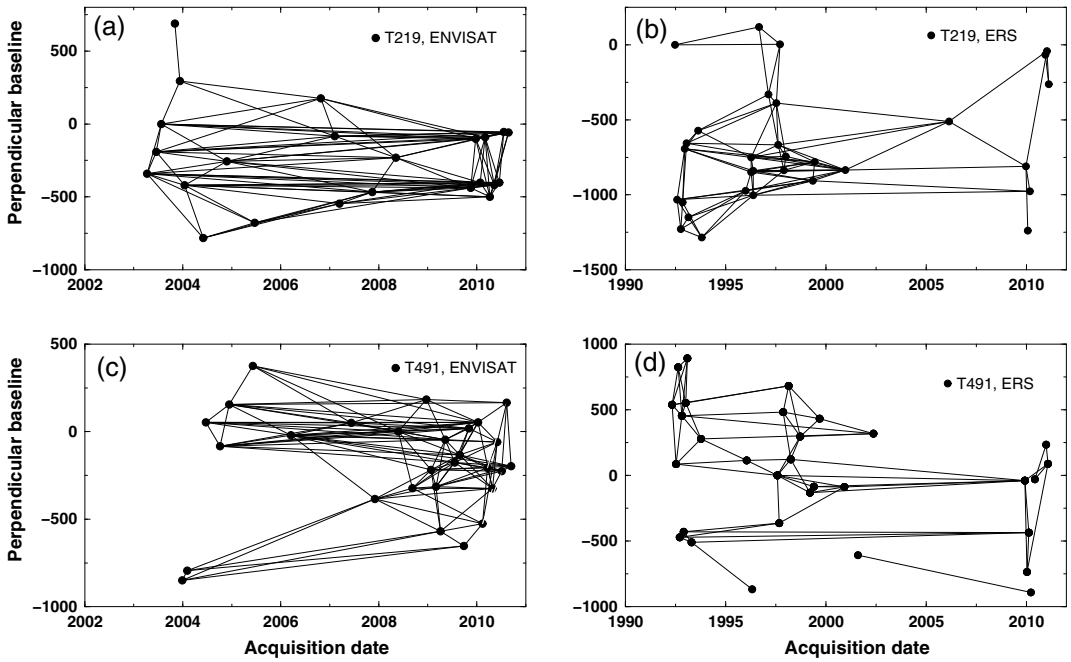

Figure 2. Plot of the SAR acquisitions (black dots) along the perpendicular baseline and time axis. The black lines represent the computed small baseline interferograms. (a) ERS T219, (b) Envisat T219, (c) ERS T491, and (d) Envisat T491.

and 88 (64, respectively) ERS interferograms on track 219 (track 491, respectively), over 800 km long segments (Figure 1). However, some acquisitions do not cover the whole segment, either north or south of the lake, or both.

The processing tools are based on the ROI_PAC software [*Rosen et al.*, 2004] with some modifications. They include successively: The computation of all Single Look Complex (SLC) images with a common band in Doppler; the projection of the Shuttle Radar Topography Mission digital elevation model (DEM) [*Farr and Kobrick*, 2000] in the radar geometry of a master image; the modeling of the geometric phase delay of all images relative to the master using DEM and precise orbits; the coregistration of all SLCs relative to the master image given the model geometric distortion in range, a quadratic transformation in azimuth and a translation in range derived from image matching; the formation of differential interferograms with common band filtering in range varying locally with the phase delay slope; the averaging of 2 pixels in range by 10 pixels in azimuth (i.e., a (2,10) multilooking) to obtain coarser differential interferograms but with reduced phase scatter. These steps allow us to reduce geometrical decorrelation, especially for perpendicular baselines reaching 500 m.

In South Tibet, south of the lake, the coherence remains quite good for relatively large time spans, except in steep terrains. Around the lake, temporal decorrelation is important for temporal baselines larger than two years; however, the phase delay signal is clearly seen when further averaging (8 by 40 pixels) is applied to interferograms. North of the lake, where freeze-thaw cycles alter the ground backscattering properties, temporal decorrelation is strong. We also observe numerous local deformation patterns of a few centimeter amplitude, associated with DEM features, along valleys or alluvial fans, which we interpret as the result of changing permafrost conditions.

The method used here to unwrap the interferometric phase delay, initially known modulo 2π, i.e., the fringe counting process, is described in Text S1 in the supporting information together with the interferogram flattening method. Four typical examples of flattened ERS and Envisat interferograms, zoomed in the lake area, are displayed on Figure 3. ERS interferograms covering the period 1993 to June 1999 do not show clear evidence of deformation centered around the lake. ERS interferograms with the second date in December 2000 show a slight subsidence pattern centered on the lake. ERS interferograms encompassing the period 2000–2006, although noisy due to temporal decorrelation, show a very clear round shape subsidence pattern centered on the lake, with a maximum amplitude, around the lake border, of approximately 4.5 mm/yr. Envisat

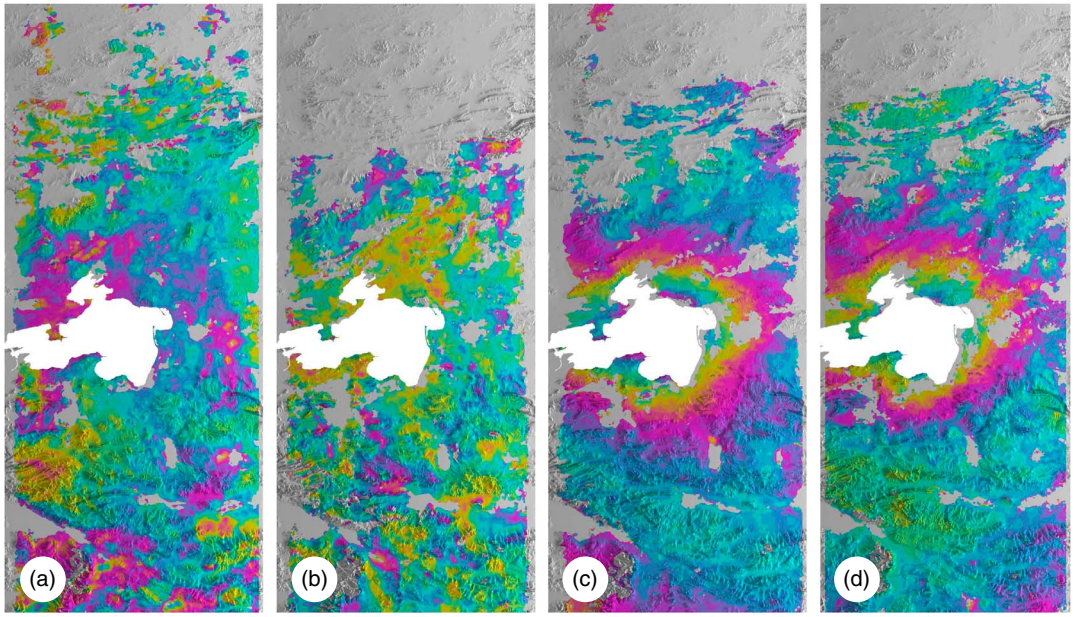

Figure 3. Examples of ERS and Envisat interferograms on track 219, centered in the lake area. One color cycle corresponds to a line of sight (LOS) delay of 2.8 cm. Note that the trends in range and azimuth have been removed from these interferograms. (a) 21 June 1992 to 17 September 1997, (b) 17 January 1993 to 9 July 1997, (c) 20 January 2000 to 23 December 2009, and (d) 9 April 2003 to 18 November 2009.

interferograms, spanning the period April 2003 to March 2010, also display a clear subsidence pattern as soon as the time span is larger than 3 years, with an amplitude similar to that observed for the ERS interferograms.

3.2. Time Series Inversion

The phase delays of unwrapped interferograms, Φ_l, are inverted pixel by pixel to solve for the incremental phase delay, $\delta\varphi_n$, of each date relative to the preceding date. The total phase delay, φ_k, are then obtained by adding incremental phase delays, assuming that φ_1 is zero. The system (equation (1a)) is solved using a least squares method. We do not regularize the system using singular value decomposition [*Berardino et al.*, 2002]. Instead, we use additional constraints provided by equations (1b)–(1d) [*Lopez-Quiroz et al.*, 2009]. We here prescribe that the evolution of the deformation, φ_k^s, is smooth in time. The phase delay temporal evolution is obtained by solving the following equations for each pixel:

$$\forall l \in [1, M] \qquad \sum_{n=i}^{n=j-1} \delta\varphi_n = \Phi_l \tag{1a}$$

$$-\alpha W_1 \varphi_1^s = 0 \tag{1b}$$

$$\forall k \in [2, N] \quad \alpha W_k \left(\sum_{n=1}^{n=k-1} \delta\varphi_n - \varphi_k^s \right) = 0 \tag{1c}$$

$$\forall k \in [1, N] \qquad \gamma \omega_k \partial^2 \varphi_k^s / \partial t^2 = 0 \tag{1d}$$

where N is the number of SAR images, M is the number of interferograms, γ is the smoothing coefficient, and ω_k are weights equal to the average time interval within the five points differential scheme used to construct $\partial^2\varphi_k/\partial t^2$. The weight, α, is set small enough so that the reconstructed total phase delay, φ_k, is not affected by the regularization, except for pixels where the set of equation (1a) is underdetermined. In the latter case only, regularization allows for a translational adjustment of disjoint portions of the phase delay time series on a single smooth temporal evolution.

The contribution to the misfit by equation (1a) is caused by interferometric network misclosure (i.e., mainly due to unwrapping error, residual phase ramp misclosure, decorrelation, and filtering effects). It is on average equal to 0.4 rad for Envisat tracks and 0.55 rad for ERS tracks. On the other hand, the contribution to the misfit by equations (1b) and (1c) is mainly due to turbulent Atmospheric Phase Screen (APS) and thus varies per

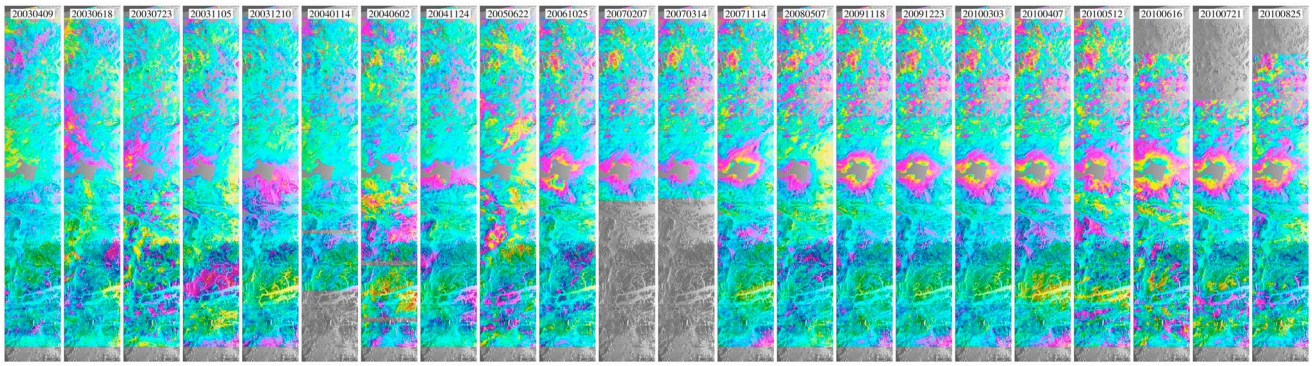

Figure 4. Snapshots of the LOS total phase delay for each acquisition date, shown in radar geometry. Gray areas corresponds either to missing data lines or to masked areas (not unwrapped because of noise). One color cycle corresponds to a LOS delay of 2.8 cm (colors evolve from blue, purple, orange, yellow, green, to cyan, away from satellite). Envisat data on track 219.

image due to meteorological conditions of the day. Therefore, the weights, W_k, applied to equations (1b) and (1c), are set inversely proportional to the amplitude of the turbulent APS of each image k, σ^k_{APS}. They allow for the smoothed time series to adjust preferentially to acquisitions with low APS. To quantify the APS amplitude, σ^k_{APS}, per image, we first compute phase variance on individual interferograms after adjusting a deformation shape. We then invert these values into image values assuming no APS covariance in between two acquisitions [*Cavalié et al.*, 2007; *Jolivet et al.*, 2012]. Finally, the number of data N is too small to efficiently separate a time dependent deformation pattern from DEM errors. The latter thus remains as noise in the reconstructed phase delay time series, φ_k.

The maps of the total phase delay time series, $\varphi_k - \varphi^s_{\mathrm{ref}}$, are shown in Figure 4 and in supporting information Figures S4–S6 for both tracks and ERS and Envisat data. To avoid the contamination of all maps by the APS of a reference image, they are displayed relative to the "smoothed" phase value of a reference image. We chose a reference date without data gaps, located at the beginning of the time series and with moderate APS.

The total phase delay time series are dominated by a rounded shape deformation pattern surrounding the lake, that is clearly visible from 2006 onward on Envisat time series (relative to end of 2003). On ERS time series, we cannot see any deformation around the lake from 1992 to 1999. Noticeable deformation starts to appear

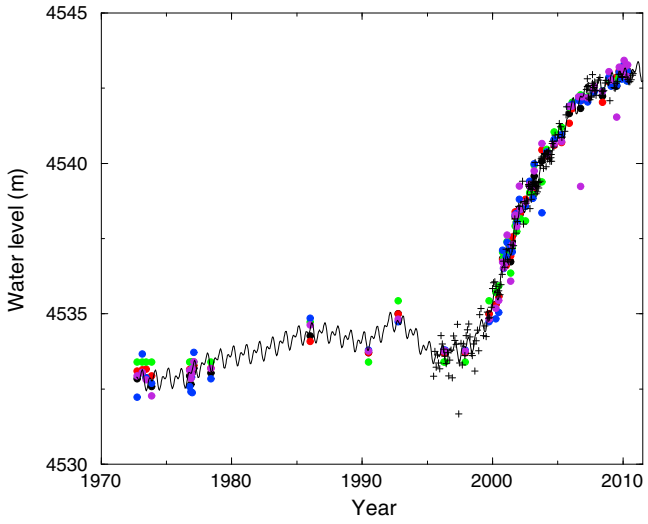

Figure 5. Evolution of the lake level from altimetric measurements (black crosses, see also Figure S1) and using area as a proxy for lake level (filled circles). The black circles correspond to the whole lake area. Colored circles (red, green, blue, purple, respectively) represent the lake area included in smaller areas covering the north, east, south, and west parts of the lake, respectively. Their spread indicates uncertainties, due to errors in lake contouring and in calibration relations. The black curve is an interpolated smooth relationship through all data points, including a constant seasonal signal, used for load reconstruction from 1972 to 2010.

in 2000–2001 and reaches 5 to 6 cm on the lake shores at the end of 2010. Other signals can be observed in total phase delay time series. North of the lake, local subsidence patterns of similar amplitude than that due to lake loading are most probably due to changing permafrost conditions. Unwrapping these patterns was difficult, especially for ERS data presenting a large data gap between 2001 and 2006 or 2009. As a result, they alter the possibility to recover the far-field deformation or reference area north of the lake. Deformation resulting from earthquakes are also clearly visible north and south of the lake. The cumulated interseismic deformation across the Gyaring Co Fault is also noticeable after 5 to 10 years.

4. Deformation Models Associated to Siling Co Lake Load Fluctuations

4.1. Water Level Variations

4.1.1. Palaeoshorelines

In the Holocene, the Siling Co Lake in Tibet had large water level fluctuations, as testified by lacustrine beaches, clearly seen up to 100 m above the present-day water level. Some of these palaeoshorelines have been dated at 30 ka, 19 ka, 12 ka, 9 ka, and 7 ka [*Li et al.*, 2009]. A compilation by *Mügler et al.* [2009] of dry and wet periods during the Holocene from the composition of lacustrine sediments in Siling Co Lake and other Tibetan lakes suggests that the latest high stand might have occurred 6 ka ago followed by oscillations of high and low stands of lower amplitude.

4.1.2. Altimetry

Altimetric measurements from Envisat and ERS satellites show a more or less stable water level from 1995 to 1999, a large water level increase of about 1.0 m/yr from 1999 to 2007, a slower rate of water level increase from 2007 to 2010, superimposed on seasonal fluctuations of about 0.7 m (Figure 5 and Figure S1 in the supporting information and references therein). The seasonal low in water level mainly occurs in May to July and the water level increases progressively during the remaining part of the year until February. The altimetric measurement in winter might be affected by ice partially covering the lake.

4.1.3. Surface Changes

In order to extend the monitoring period of the lake level, we use all available cloud free LANDSAT images. Ten images in 1972–1978, one image in 1986, and one image in 1990 allow us to depict, however, sparsely, the water level evolution before the ERS-ENVISAT study period. The remaining images span the period 1999 to 2010. Except for the earliest images, the resolution is of 30×30 m^2. The evolution of the lake contour, further described in the supporting information Text S2 (Figure S2), shows the progressive inundation of a valley in the northern part of the lake, a progressive runup on the lake former shorelines on the east, and an increase in lake area on the west.

To compensate for the lack of LANDSAT images from 1990 to 1999, we also manually contoured the lake on four ERS SAR images (on 4 October 1992, 9 April 1996, 14 May 1996, and 26 November 1997), aided by coherence maps obtained from 1 month or 1 day interferograms when available. We find that the lake contour in the 4 October 1992 scene follows that of the September 1999 LANDSAT image, whereas for the three other ERS scenes it follows that of the June 1990 LANDSAT image.

4.1.4. Reconstructed Water Level Curve From 1972 to 2010

We convert the lake area into lake level using calibration relations between area and elevation. They are obtained for the total lake area and separately for four subareas of the lake (see supporting information Text S2 and Figure S3). Figure 5 displays the area evolution converted to lake level, together with superimposed altimetric measurements. Because the lake area before 1995 did not vary a lot below or above the 1995–2010 limits, only small errors should arise from the choice of the calibration relation. The seasonal signal, with marked lake level decreases during the end of spring, is also clear in the area evolution. For the period 1972–1999, although less constrained, the rate of water level increase is inferred to be low, <0.05 m/yr, in comparison to the 0.7 m/yr rate inferred for the period 1999–2008.

Using all altimetric measurements and area estimates, we produce an interpolated temporal evolution of the lake level composed of a smooth pluriannual curve on which is added a constant seasonal signal, made of two adjusted sinusoids with 1 year and 6 month periods. The standard deviation of altimetric and calibrated area data around this interpolated curve is 30 cm and 20 cm, respectively. Considering a measurement redundancy larger than a factor 5 for the period 1995 to 2010 (see Figure 5), the 1σ uncertainty on the reconstruction of the lake elevation curve through time is estimated to be less than 15 cm. Larger uncertainties are expected for the period 1972–1994, where only few LANDSAT data of lower quality are available. Assuming that no

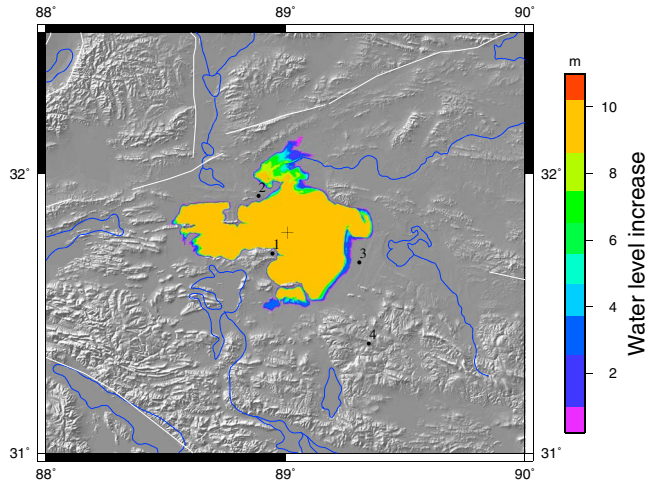

Figure 6. Map of the water level change from January 1992 to June 2011. The cross indicates the gravity center of the mass change. Black dots referred by numbers are placed at increasing distance from the gravity center and are used for sensitivity tests.

abrupt excursions in lake levels took place in the years where we have no measurements, we propose semiquantitatively an uncertainty of ±70 cm on the reconstructed lake level curve in the period 1972–1994 (see supporting information Text S2).

4.1.5. Origin of Lake Level Variations

The reasons explaining the 1999–2010 water level increase are debated and include glacier melting, decrease of potential evapotranspiration, permafrost melting, or increased precipitation. Siling Co Lake has the largest inland drainage in Tibet (45×10^3 km^2), that includes areas prone to permafrost fluctuations [*Cheng and Wu*, 2007] and one large mountain glacier, the PurogKangri ice field. The interannual trend in lake level may be related to the warming of the Tibetan Plateau observed since 1965 by meteorological stations in Tibet. This warming averages to about 0.36°C/decade during the period from 1961 to 2007 [*Wang et al.*, 2008]. The average warming rate appears to increase since 1995. Precipitation in the eastern and central parts of the Tibetan Plateau also increased over the past several decades [*Xu et al.*, 2008]. *Yao et al.* [2007] or *Wu and Zhu* [2008] argue that the recent water level increase in Siling Co and other nearby lakes is partly due to glacier retreat and partly due to increased precipitation. However, analysis of in situ climatic data shows that the increase in lake level is better correlated to the recent temperature increase than to precipitation variations [*Meng et al.*, 2011]. Alternatively, permafrost degradation in Tibet-Qinghai Plateau, with the rising by tens of meter of its altitudinal limit [*Cheng and Wu*, 2007; *Kang et al.*, 2010] is a plausible major contributor to the lake water level rise.

4.1.6. Lake Load

The lake load (Figure 6) is built from both the progressive area change with time and the lake level curve, from 1972 to 2012 every 0.5 yr. The lake area, and its change with time, also includes a small lake to the SE of the main lake, that appears to progressively widen with time and becomes connected to the main lake after 2004. The relatively large lake located southwest of Siling Co, presents a constant water level and is therefore excluded from the load. Two other small endorheic lakes located east and northwest of Siling Co present varying areas, including periods where they dry completely. The ground reflectivity around these lakes in Landsat images suggests the presence of salt deposits. These shallow small lakes are thus probably extremely sensitive to evaporation. Because of their small size, their episodic filling, and their unknown water level history, these lakes are excluded from the load computation.

4.2. Models of Load-Induced Deformation

4.2.1. Numerical Derivation

The response to surface loading is computed in a compressible layered Maxwell viscoelastic medium. The flat Earth equation of motion, for small displacements and when autogravitating terms are negligible, but including prestress advection is

$$\nabla \cdot \tau - \rho_0 g_0 \nabla u_z + \rho_0 g_0 (\nabla \cdot \vec{u}) \vec{e}_z = 0 \tag{2}$$

where τ is the stress perturbation, ρ_0 and g_0 are the initial density and gravity acceleration depending on depth z, $\vec{u}$ is the displacement field, u_z is the vertical displacement, positive upward, and $\vec{e}_z$ a unit vector along the vertical axis [*Cathles*, 1975]. As the load τ^0_{zz} is applied on a free flat surface, the above equation plus the constitutive relationships are linear and are solved by a spectral method, i.e., by 3-D Fourier decomposition on the horizontal (x, y) plane and in time t, and with numerical integration of a propagation matrix along the vertical axis [*Cathles*, 1975; *Cavalié et al.*, 2007]. Elastic moduli are replaced by equivalent elastic moduli depending

Table 1. V_P, V_S, and Density Structure For Siling Co Lake

Depth (km)	V_P (km/s)	V_S (km/s)	ρ ($\times 10^3$ kg/m^3)
0–5	4.2	2.5	2.4
5–32	6.1	3.6	2.65
32–45	6.7	3.8	2.8
45–65	7.3	4.1	3.0
65–250	7.8	4.4	3.3

on the pulsation ω. Note that the Fourier transform in time, rather than the Laplace transform, is here also used in the time axis. Boundary conditions are a vanishing displacement at the box base and a vanishing shear stress at the top. Kernels for the surface displacement $\vec{u}(\vec{k},\omega)$, where $\vec{k}$ is the wave number, are convolved to the surface load decomposition and yield by inverse Fourier transform the complete displacement field. The spectral method implies periodic boundary conditions along the horizontal and time axis. Thus, the model space (in (x, y, t)) must be large enough for the solution to be insensitive to these periodic boundary conditions. More details on the numerical setup can be found in *Cavalié et al.* [2007].

4.2.2. Model Setup

We compute the purely elastic and viscoelastic surface deformation associated with the lake load fluctuations. We thus place the 2-D surface load varying with time on top of a cube with layered viscoelastic properties. In all cases, the elastic Lamé parameters are calculated from the V_P, V_S, and ρ structures given in Table 1 and derived from the seismic experiments near the Siling Co Lake [*Zhao et al.*, 2001; *Haines et al.*, 2003]. They are well constrained but represent the elastic response at seismic wave speed.

Except for resolution (see supporting information Text S3) and sensitivity tests, runs are performed on a space of dimensions $500\times500\times500$ km^3, with an horizontal and vertical spacing set to 1 km and 500 m, respectively. For most viscoelastic cases, we choose a computation period of 768 years (equal to $2^9\times3\times0.5$ y), set arbitrarily from 1562 to 2309.5, with one step every 0.5 year. The load is set to zero before and in 1972 and set back to zero after 2012. The maps of load changes since 1972 are applied from 1972 to 2012.

We test the following four models, a purely elastic model and three series of viscoelastic models. For each of these three cases, the viscosity structure is defined only by two parameters: the top layer elastic thickness, H_e, and the middle to lower crust viscosity, η. In the three cases, the top layer down to H_e has a viscosity large enough (10^{25} Pa s) to behave completely elastically. In models (A), it is underlained by a viscoelastic half-space of constant viscosity. In the ductile channel models (B), the lower crust viscosity, η only applies between H_e and the Moho, and the uppermost mantle viscosity below the Moho (65 km) rises again to 10^{25} Pa s. Finally, models (C) present as in models (B) a low-viscosity channel in the crust, but the asthenosphere viscosity is set below 90 km to 10^{18} Pa s. The surface displacement fields at each acquisition date are projected along LOS and in radar geometry.

We present in Figure 7 four examples of forward models of surface displacement between 1992 and 2010. The elastic model presents a subsidence pattern restricted to the lake vicinity with high gradients on the lake shore, reaching about 2.8 cm. The displacement amplitude is by far larger below the lake than on its shore. However, there are no islands or peninsulas which would allow displacements close to the lake load center to be measured. All three viscoelastic models presented in Figure 7 have predicted surface displacements in 2010 relative to 1992 about twice as big as that predicted for the purely elastic model. The subsidence also decays more slowly away from the lake borders. The difference between the elastic and viscoelastic models is a rounded shape, similar to that of a point load laid on an elastic layer of finite thickness. The radius of this additional deformation increases with the elastic thickness. The largest wavelengths are, however, damped for "low-viscosity channel" models (B), which act as a band-pass filter. On the other hand, elastic bending of a thin uppermost lithospheric mantle above a low-viscosity asthenosphere (C) produces additional very large wavelength deformation. The parameters chosen for the three viscoelastic models shown in Figure 7 are such that they have similar subsidence pattern and gradients close to the lake (first 100 km from the lake center) but different large-scale patterns.

4.2.3. Sensitivity to Elastic Parameters

We construct sensitivity kernels to elastic parameters by decreasing the Lamé moduli of the reference elastic model by a factor 2 in 5 km thick sublayers (keeping the same Poisson ratio). For each modified model

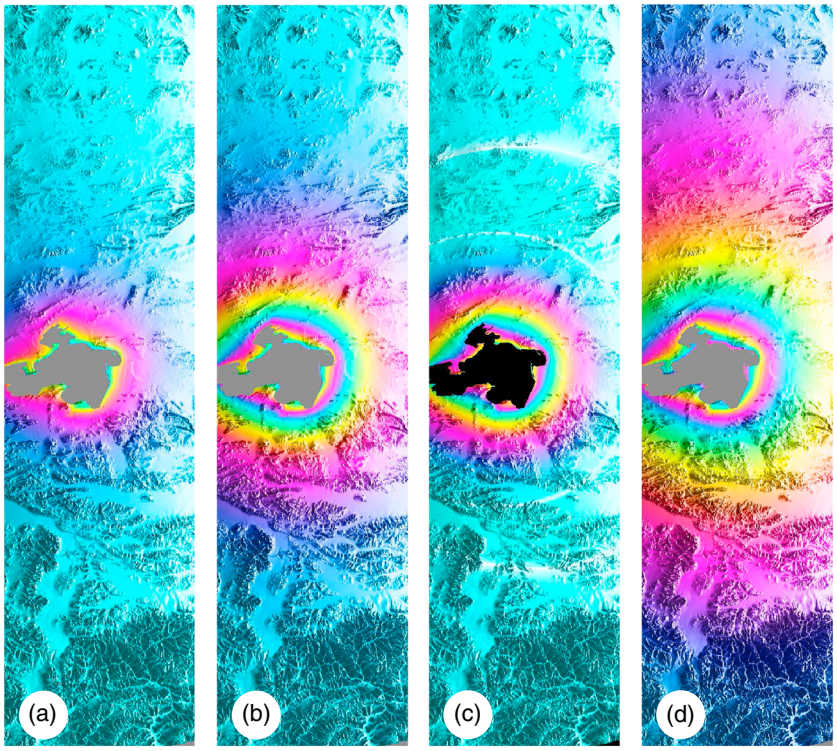

Figure 7. LOS displacement models in radar geometry (track 219, see location on Figure 1) computed for four different viscoelastic structures. The subsidence around the lake, between early 1992 to end 2010, is shown in a wrapped color scale (one color fringe for 2.8 cm of LOS displacement). (a) Purely elastic model. (b) Model (A) made of a half-space viscoelastic layer with a viscosity of 6×10^{18} Pa s underlying a purely elastic layer of 20 km. (c) Model (B) with a viscoelastic layer ($\eta = 2 \times 10^{18}$ Pa s) between 30 and 65 km sandwiched between two purely elastic layers. (d) Model (C) with a viscoelastic layer ($\eta = 7.5 \times 10^{18}$ Pa s) between 15 and 65 km sandwiched between two purely elastic layers, underlained below 90 km by a viscous half-space of viscosity 10^{18} Pa s.

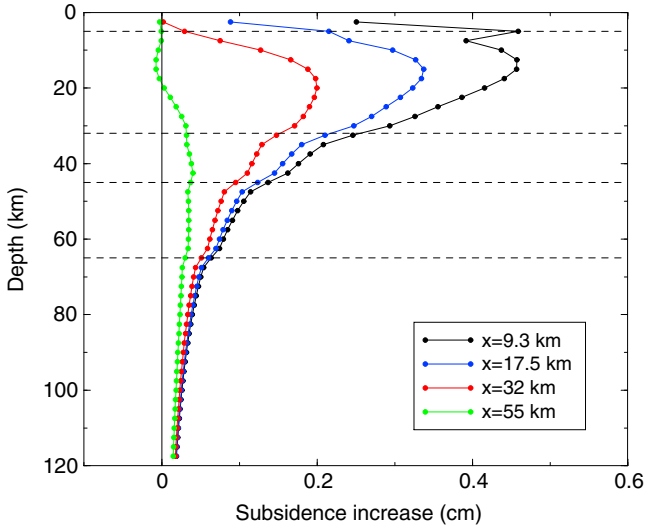

Figure 8. Depth sensitivity to elastic parameters. Shown on the horizontal axis is the excess subsidence computed when decreasing the Lamé parameters by a factor 2 in 5 km thick sublayers (the vertical axis refers to the center of each modified sublayer). The horizontal dashed lines indicate the elastic layering of the reference model (see Table 1). See Figure 6 for the four points location.

(defined by the middle depth of the modified sublayer), we compute the subsidence increase between 1992 and 2010 for four points located at various distances from the lake load gravity center (Figure 8). By constructing these curves, we implicitly assume that the surface displacement due to the deformation in a given sublayer is inversely proportional to its Lamé parameters, independently of the other sublayer elastic moduli. This is of course not exactly true; nevertheless, the curves give a good idea on the depth sensitivity to elastic parameters. The point located on the shore and the closest to the lake load center of mass has the shallowest sensitivity, however, remaining small for the top 5 km thick sediment layer. The other curves show that the vertical displacement probes mostly the first 40 km part of the crust with limited relative weight put on the first 10 km. In other

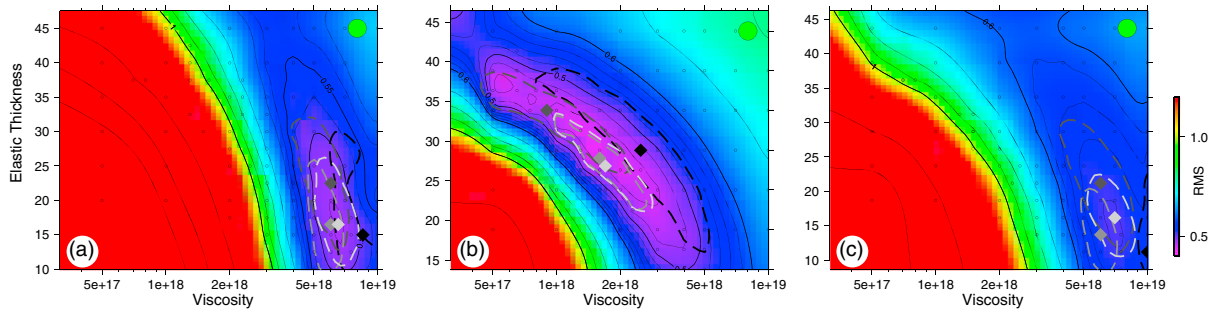

Figure 9. Misfits between the time series of phase delay maps and the viscoelastic models, shown as a function of lower crust viscosity and elastic thickness. Each small circle corresponds to a model computation. (a) Model series (A) with a purely elastic half-space overlying a viscoelastic half-space. (b) Model series (B) with a viscoelastic layer restricted to the lower part of the crust. (c) Model series (C) with a low-viscosity asthenosphere added. The contoured color maps represent the misfit function for all acquisitions, whereas the dashed thick lines contour the low misfit area for restricted sets of acquisitions (white: T219 Envisat, taken at 0.11, 0.09, and 0.14, for Figures 9a to 9c, respectively; light gray: T491 Envisat, taken at 0.20, 0.18, and 0.22, for Figures 9a to 9c, respectively; gray : T219 ERS, taken at 0.55, 0.54, 0.55, for Figures 9a to 9c, respectively; dark gray: T491 ERS, taken at 0.86, 0.78, and 0.93, for panels Figures 9a to 9c, respectively). Individual best fit positions are shown with diamonds. The colored circle displayed on the top right corner of each panel is the misfit for the purely elastic model.

words, decreasing Lamé coefficients by a factor 2 in the first 10 km will be very far from producing a factor 2 increase in subsidence. Sensitivity to moduli below 40 km is small because elastic stresses at this depth have strongly decayed.

5. Comparison Between InSAR Results and Model Predictions

5.1. Best Fit Adjustments to the Total Phase Delay Time Series

The maps of the total phase delay time series, shown in Figure 4 and in supporting information, are compared to the model displacements projected into radar geometry and along the LOS, and referenced to the same dates as the observations. To preserve all possible lake loading signal, we use the time series, ϕ_k, i.e., obtained without temporal smoothing or turbulent APS removal. The comparison is performed at each time step for the elastic model and for the three viscoelastic models A–C (described in section 4.2.2) with varying elastic thickness and lower crust viscosity and is limited to a 200 × 100 km^2 area surrounding the lake.

The residuals, data minus models, are quantified as described below. For each acquisition k, we first adjust and remove a "twisted" plane, in the form $ax + by + cxy + d$, where x is range and y is azimuth, to the difference between the data and model maps, and then compute the residual root-mean-square standard deviations, RMS^k. Clear outliers, larger than 2.5 times RMS^k, are iteratively removed in this adjustment process, and the RMS^k values are computed again with edited outliers. Iterations stop when convergence is reached. The outlier removal procedure lowers the RMS^k values for models presenting a large misfit to observations; however, for models close enough to the best fit models, it favors models giving residuals well distributed around zero. The "twisted" plane adjustment, restricted to the lake area once the model is removed, is here different from the large-scale interferogram flattening (Text S1.3 in the supporting information) that was previously applied to the 800 km long track after masking the lake area.

The total misfit function, m, plotted in Figure 9 is then defined as

$$m = \frac{1}{N} \sum_k \frac{\mathrm{RMS}^k}{\sigma^k_{APS}} - 1 \tag{3}$$

where N is the number of acquisitions and m is computed either separately for each of the four tracks or jointly for all acquisitions. Each acquisition is normalized by its estimated noise amplitude, σ^k_{APS} to avoid overfitting the noisiest images. In principle, a successful model could adjust the data within its estimated noise dispersion, σ^k_{APS}. Such a "complete" adjustment means $m = 0$, as -1 is added to equation (3). However, residual phase screens present atmospheric noise patterns correlated over approximately 30 km [*Cavalié et al.*, 2008; *Jolivet et al.*, 2012]. They have therefore a good chance to be partially correlated to a bowl shape function centered on the lake. This correlated contribution is removed when computing σ^k_{APS} independently for each acquisition, as described in section 3.2, but remains in residuals computed from time series of data and model.

Two-layer model (A) and four-layer model (C) with a low-viscosity asthenosphere both yield a best fit elastic thickness of 10–25 km and crust viscosity of 6–8 × 10^{18} Pa s; however, the misfit is lower ($m = 0.475$) for

the two-layer model than for the four-layer model ($m = 0.518$). The low-viscosity channel model (B) has a larger elastic thickness (25–35 km) but a lower viscosity ($1–3 \times 10^{18}$ Pa s). As the viscous channel acts as a band-pass filter, the suppressed large-wavelength response is compensated by a larger elastic thickness and lower viscosity. The misfit appears lower ($m = 0.450$) for the viscous channel model than for the two other models, suggesting that the relatively focussed deformation field precludes any significant deep viscous flow. We will further discuss in subsection 5.3 how significant this point is by a spatial analysis of the deformation pattern.

A strong trade-off is observed between the elastic thickness and the viscosity for the viscous channel model. This trade-off is, however, less prominent for the two other models for which the viscosity remains near 7×10^{18} Pa s for all elastic thicknesses between 10 and 25 km. Note also that the four best fit locations (η, H_e), computed independently for each track, are consistent, except for the ERS track T491 which is slightly offset toward larger viscosity. The phase delay maps for this track are also noisier than for the three other tracks. The misfit using the purely elastic model is twice as large ($m = 0.891$) than for the viscoelastic models. Therefore, a significant viscous flow in the middle to deep crust is needed to explain the observations. To further discuss this result and argue by how much it is data supported, in the next two subsections we decompose the spatiotemporal signal into the amplitude of the deformation through time and the spatial shape of the deformation.

5.2. Temporal Evolution of the Deformation

The temporal behavior of the ground motion allows us to discriminate instantaneous elastic response to stress from a continuing viscous response to stress. It is well-known that an applied step-like load will produce a subsidence evolution with a characteristic timescale proportional to the viscosity. Here, the lake level increases steeply after 2000, but its rate decays after 2007, corresponding to a concave evolution with time. A nonnegligible viscous flow over a decadal timescale should then produce a response being more linear, or even first convex with time, before stress completely relaxes.

To discuss this effect, one must extract the deformation amplitude with time with an enhanced signal to noise ratio. Plotting phase delay time series for single pixels is clearly insufficient. We project interferograms on a spatial deformation template (denoted $G(x, y)$). We assume that the deformation $D(x, y, t)$ can be written as $D(x, y, t) = A(t) \times G(x, y)$. All deformation shapes plotted in Figure 7 have been tested as templates, but results will be shown later only for the elastic template G_e and the ductile channel model template G_v.

The following linear relation is adjusted to each interferogram, $\Phi_{ij}(x, y)$:

$$\Phi_{ij}(x, y) = ax + by + cxy + dy^2 + e + A_{ij} \times G(x, y) \tag{4}$$

where x and y are the range and azimuth, respectively, and $ax + by + cxy + dy^2$ corresponds to an adjusted phase ramp (residual orbit or atmospheric contribution). The coefficients a, b, c, d, e, and A_{ij} are obtained by least squares inversion on a 200×100 km^2 area centered on the lake. The joint inversion allows to take into account trade-offs in the estimation of the various terms. Standard deviations on A_{ij}, σ_A^{ij}, depend on the number of independent data used in the inversion. As atmospheric noise is spatially correlated, we arbitrarily set this number to 9 in the 200×100 km^2 area around the lake.

The amplitudes, A_k, at acquisition times k are then obtained by inverting the system: $A_{ij} = A_j - A_i$ and $A_1 = 0$. We find that the values of A_{ij} obtained for individual interferograms are consistent (the system misclosure is about 5%). All network residuals, $A_{ij} - (A_j - A_i)$, for a given image are added and averaged in a root-mean-square sense, providing a misclosure error estimate per image, Err_k. Furthermore, standard deviations, σ_A^{ij}, are also inverted into time series, using $\sigma_A^{ij} \approx \sigma_{iA}^{i} + \sigma_{iA}^{j}$. We then add the two sources of error on A_k to get

$$\sigma_A^k \approx \sigma_{iA}^k + \mathrm{Err}_k \tag{5}$$

The temporal inversion is performed separately for the four data sets (ERS and Envisat and two different tracks) (Figure 10a). Smoothing constraints weighted by σ_A^k are then used to compute the translations between independent data sets that minimizes the offsets between the four time series (Figures 10b and 10c).

The obtained temporal evolutions, $A(t)$, are very similar for both elastic $(G_e(x, y))$ and viscoelastic $(G_v(x, y))$ shapes. However, $A(2011) - A(1992)$ values obtained using $G_e(x, y)$ reach 2.7 (Figure 10b), whereas it reaches

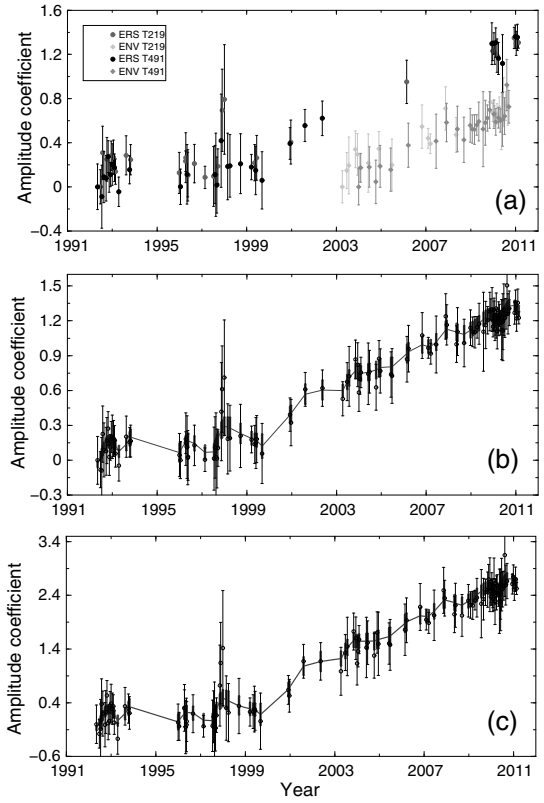

Figure 10. Temporal evolution of the deformation amplitude, $A(t)$. (a) Shown independently for each track, with σ_A error bars. The spatial shape $G(x, y)$ used to compute $A(t)$ is obtained for the three-layer model (series B) shown in Figure 7c. (b) As in Figure 10a but a translation is adjusted to each independent time series that optimizes the curve smoothness. The solid smooth curve includes thick error bars, computed for a certain degree of smoothing, that result from noise simulations on A_k values. (c) As in Figure 10b but using the spatial shape of the elastic deformation (Figure 7a) to compute $A(t)$.

1.2 using G_v. This means that a factor 2.7 must be applied to the elastic model prediction to scale with the observed deformation. In both cases, there is little cumulated deformation from 1992 to 1999. From 2001 to 2011 the subsidence rate remains more or less constant. Two dates at the end of 1997 present anomalous values for A, but with large error bars. Visualization of the phase delay maps (Figures S5 and S6 in the supporting information) shows for both dates a large and wide NE-SW trending feature that presents a small correlation with the deformation pattern, which must explain the perturbation in A.

The temporal sampling of SAR acquisitions is irregular, and intuitively, one can infer that where sampling is dense, individual assessments of A_k values can be combined to produce a temporally averaged value with a smaller error bar. We thus compute a smoothed curve, A^s_k, using all individual data inversely weighted by their standard deviations (Figures 10b and 10c). The distribution of $A_k - A^s_k$ values shows that 85% of smoothed values fall within the σ^k_A error bars. We then compute new error bars on smoothed A^s_k values based on random simulations of noise with an amplitude constrained by the individual standard deviations σ^k_A. The new standard deviations on A^s_k values are, not surprisingly, smaller for densely sampled acquisitions than for loosely sampled ones (Figures 10b and 10c).

In order to compare viscoelastic model predictions to the observed smoothed amplitude values, A^s_k, we apply exactly the same procedure to the model deformation maps in radar geometry and along LOS direction (i.e., equation (4)). The misfit between predicted and observed curves, using the viscoelastic shape $G_v(x, y)$, is shown in Figures 11a and 11b, for the two-layer model and the viscous channel model, respectively. The fits are very good (RMS lower than 0.04), and clearly better than that obtained for the elastic model, even when the latter is scaled to fit the observations. The best fit location is the same or very close to that obtained in Figures 9a and 9b.

In Figure 12a, the evolution $A^s(t)$, computed using $G_e(x, y)$, is compared to the unscaled and scaled elastic model predictions. The latter, in phase with lake level variations, presents a clearly more concave shape than the observation. By contrast, end-members viscoelastic models which present a good fit to the observed amplitude also have a temporal evolution that closely matches the observed deformation trend (Figures 12b and 12c). To illustrate the sensitivity to elastic thickness or viscosity, other examples with either higher or lower predicted amplitudes are also shown. We conclude that the data temporal evolution favors the existence of a nonnegligible ductile contribution that increases approximately linearly with time.

The above remarks and conclusions also hold when using other viscoelastic shape functions $G(x, y)$, when removing the term in y^2 in equation (4), or when using a different level of smoothing. The solution using a viscoelastic shape function close to the best fit model is preferred for consistency, but the best fit (H_e, η) domain remains unchanged when using other "reasonable" viscoelastic models. The inclusion of a quadratic term in y, that partially trades-off with large-wavelength deformation patterns, appears surprisingly to slightly stabilize the A_k time series, and lowers the deformation amplitude by 5% to 10% leaving the shape of $A^s(t)$ unchanged.

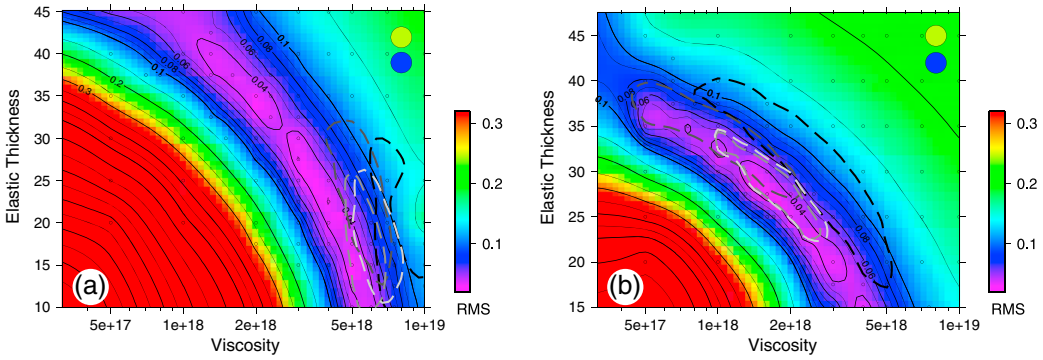

Figure 11. Misfits between the temporal evolution of the deformation amplitude, $A(t)$, and the model amplitude, $A^m(t)$, computed with the same procedure (the spatial shape used here is the three-layer model shown in Figure 7c). Each small circle corresponds to a model computation. (a) Model series (A) with a purely elastic half-space overlying a viscoelastic half-space. Panel (b): Model series (B) with a viscoelastic layer restricted to the lower part of the crust. The dashed thick lines are the same as in Figure 9. The colored circles displayed on the top right corner of each panel show the misfit to the (top) elastic model and (bottom) elastic model scaled with a factor of 1.85.

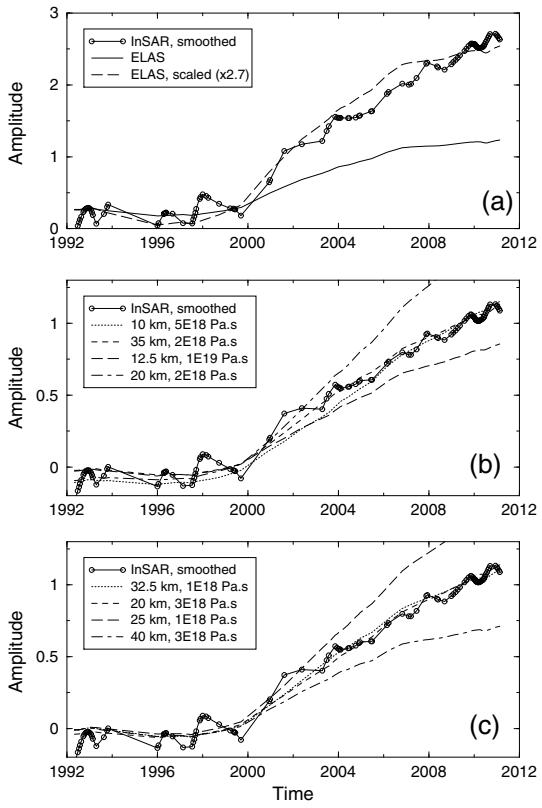

Figure 12. Comparison between the temporal evolution of the deformation and that of the model. The spatial template used here to compute A is in Figure 12a the purely elastic model (Figure 7a) and in Figures 12b and 12c the three-layer model (Figure 7c). (a) Purely elastic model and scaled elastic model (factor 2.7). (b) Two-layer models (A) using end-members best fit parameters (5×10^{18} Pa s, 10 km to 2×10^{18} Pa s, 35 km) or models yielding lower (1×10^{19} Pa s, 12.5 km) or larger (2×10^{18} Pa s, 20 km) amplitudes. (c) Three-layer models (B) using end-members best fit parameters (1×10^{18} Pa s and 32.5 km to 3×10^{18} Pa s, 20 km) or models yielding either lower (3×10^{18} Pa s, 40 km) or larger (1×10^{18} Pa s, 25 km) amplitudes.

Including this term partly accounts for unknown large-wavelength atmospheric noise and orbit errors, but only very slightly offsets the final results toward larger viscosity values. Less smoothing yields higher misfits but does not change the best fit (H_e, η) domain. Hence, our conclusions appear robust with respect to the implementation details of the amplitude extraction.

5.3. Spatial Shape of the Deformation

As seen in Figure 7, the spatial extent of the predicted deformation depends on the existence of deep ductile flow, and thus on the viscosity stratification. A very large-scale concentric deformation pattern, centered on the lake load, is indicative of a deep ductile flow on a decade timescale, and thus a low-viscosity uppermost mantle. However, large-scale atmospheric patterns, orbital errors, and permafrost effects to the north limit the accuracy of individual InSAR measurements of large-wavelength deformation patterns. To discuss the existence of a broad-scale deformation pattern associated with lake loading, we extract the spatial shape of the deformation pattern on phase delay maps flattened using phase information collected outside the deformation area and adjusted with a quadratic term in azimuth now constrained on a longer part (≥400 km) of the track.

The shape, $G_o(x, y)$, of the deformation is extracted from time series of phase delay maps (Figure 4 and Figures S4–S6 in the supporting information) by computing the linear regression coefficient between the phase

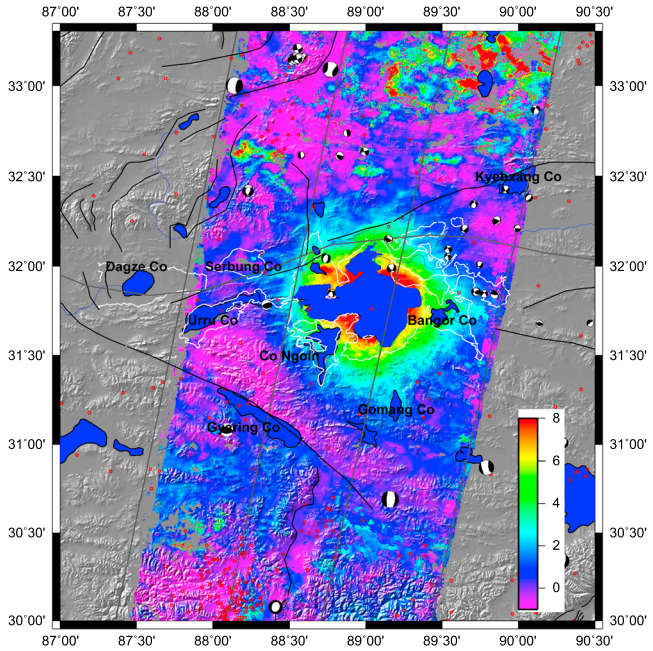

Figure 13. Spatial shape of the LOS displacement around the lake. Its amplitude corresponds to the cumulated ground displacement between 1999 and 2009 and is expressed in radians (8 rad corresponds to 3.85 cm of subsidence). The four maps obtained independently for the two ERS and Envisat tracks have been averaged where necessary. The average include typically four values in the track overlap area, and two on the sides, except in areas of low coherence where less data are available. Before averaging, all values have been rescaled along a single incidence angle of 22.4°assuming vertical deformation. The white line is drawn 50 m above lake level.

values and the temporal behavior of the deformation $A^m(t)$, weighted by $\sigma_{\mathrm{APS}}(t)$. This calculation is done iteratively, with a progressive downweighting of very large outliers in time, and with an iterative adjustment of each phase delay map reference value using phase residuals. The shape $G_o(x, y)$ is different from a velocity map, as $A^m(t)$ is not linear in time, especially for ERS data for which $A^m(t)$ is mostly flat up to 1999. However, its values (in the range 0 to 10 rad) are a proxy for the cumulated displacement in LOS between 1999 and 2009. For comparison, we apply exactly the same procedure (including weights) to the predicted phase delay maps in LOS. Once the shapes are extracted for each time series, they are assembled in Figure 13, after projection along a single incidence angle and assuming vertical displacement. Taking into account across-track variation in incidence angle allows for a very good agreement in the overlap area of tracks 219 and 491.

Figure 13 shows a deformation pattern dominated by lake loading and with a limited spatial extent. To the north, one can observe patches of subsidence associated with permafrost changes. The effect of the Gyaring Co Fault is also evident south of the lake. To discuss quantitatively the spatial extent of the observed deformation, we present in Figures 14a and 14c a radial profile away from the lake load center of mass. It shows a continuous deformation decrease up to 80 to 90 km, then a stable value or even possibly a slight increase. Comparison with best fit models shows that the two-layer model prediction clearly over estimates displacements from 60 to 110 km. On the contrary, the shape of the viscous channel model is in very good agreement with observations. A plot of the observed versus predicted LOS displacement (Figures 14b and 14c), zoomed in the range 0.5 to 2 rad, shows that the three-layer model better predicts the far-field deformation pattern. These plots demonstrate that the better RMS obtained above (section 4.1 and Figure 9) for the viscous channel model is significant and that we can exclude a deep ductile flow contribution to the lake rebound at this geodetic timescale.

Density plots also underline dispersion due to the other sources of deformation already discussed (permafrost, interseismic deformation). In elongated areas along a few parts of the lake shores, the model slightly but significantly overestimates the observed displacement. The same phenomenon is observed along the lake Mead shores [*Cavalié et al.*, 2007]. We interpret this as small relative ground uplift due to increased fluid pressure in sediments nearby the shore.

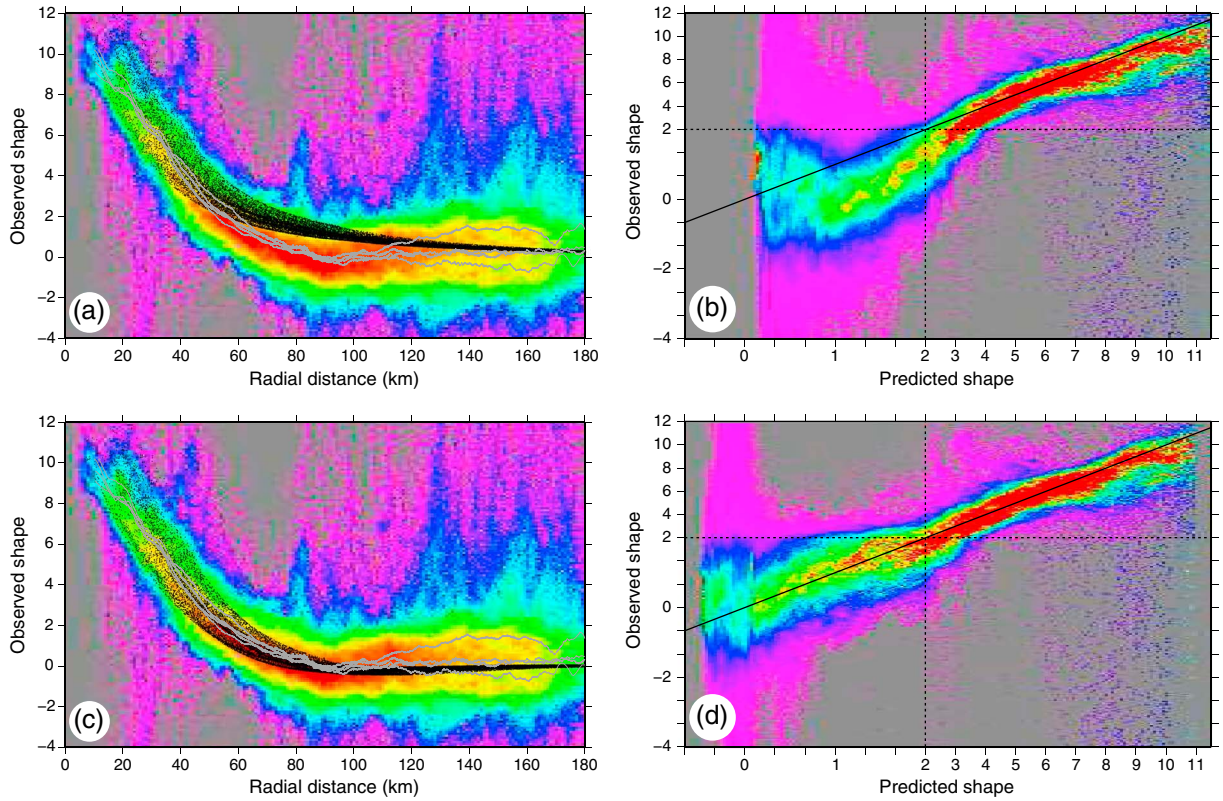

Figure 14. Density plots of the spatial pattern of the deformation compared to best fit model predictions. The four tracks spatial patterns contribute to the density calculation, shown with a logarithmic color scale. The "shape" amplitude, along the LOS and in radian, is a proxy for the cumulated ground displacement between 1999 and 2009. (a and c) The deformation is displayed as a function of the distance to the lake load center of mass. The four gray curves are the median for the four tracks separately. Black dots represent the model prediction. (b and d) The deformation is displayed as a function of the predicted displacement, with a zoom for displacement values below 2 rad. Here the color coding corresponds to the logarithm of the density normalized within bins in the x direction. The black curve is the $x = y$ line. Figures 14a and 14b show the comparison with a best fit two-layer model ($H_e = 15$ km; $\eta = 7.5 \times 10^{18}$ Pa s). Figures 14c and 14d shows the comparison with a best fit three-layer model ($H_e = 30$ km; $\eta = 1.6 \times 10^{18}$ Pa s).

6. Discussion

Given the change in water load on Siling Co Lake and the elastic moduli derived from seismic experiment studies, the elastic model does not fit the observed deformation. First, it underpredicts the deformation amplitude by a factor 1.9 to 2.7, depending on how the data are weighted. Second, the elastically deformed zone is too narrow and the displacement gradient too steep around the lake shore. Third, the instantaneous elastic response to loading does not match the observed temporal evolution of the deformation, which seems to lag behind lake level changes. However, before invoking viscoelastic rheologies for the Tibetan crust, one must discuss both the load construction and the choice of elastic moduli employed for the elastic model prediction.

6.1. Load Construction

We consider that the redundancy of altimetric measurements together with the calibration of LANDSAT derived lake surfaces yields an uncertainty on lake level of about ±15 cm, i.e., 1.5% of lake level change, which is negligible compared to other sources of error. The largest source of error on load construction is underground water for which we have no in situ data at all, and possibly contribution by other smaller lakes. We discuss below these possible contributions.

The Siling Co Lake has the largest drainage basin of all endorheic lakes in Tibet. Its level increase reflects the increase in water volume collected within the entire drainage basin, regardless of its origin (precipitation, glacier melting, and permafrost evolution). By contrast, areas that do not accumulate water through drainage should have a water table increase much smaller than the Siling Co level increase. As a result, changes in the water table level near the lake should largely be controlled by the water level changes in the lake and the progressive hydraulic diffusion in sediments away from the lake shore. Similarly, subsurface seepage around artificial reservoirs, although largely unconstrained, is believed to have a nonnegligible contribution to the

reservoir water budget, possibly reaching 30% in 30 years [*Chao et al.*, 2008]. Valleys or depressions might also be areas of accentuated underground water accumulation, unless the water table elevation is limited by surface rivers or by lakes with outlets. These low areas, with less relief, are approximately contained within the contour line drawn at an elevation of 50 m above the Siling Co Lake in Figure 13. Within this area, two relatively large lakes to the south (Co Ngoin) and to the east (Urru Co) have outlets toward Siling Co and present no water level change [*Zhang et al.*, 2011]. Also in the south, Gomang Co water level is controlled by its outlet toward Siling Co. To the east is the Bangor Co Lake, at an elevation 20 m below that of Siling Co, which displays episodic filling in LANDSAT images but no systematic increase since 2000. Hydraulic diffusivity between the two lakes should not be large enough for both lake levels to present similar evolutions. A few other small endorheic lakes in the vicinity (at 60 km, Serbung Co, to 100 km, Dangze Co, from lake load center of mass) display water level increase at a rate of ~0.4 m/yr [*Zhang et al.*, 2011]. Their water level may be associated with hydraulic head changes in the surrounding sediments. Their load may possibly be responsible for small additional subsidence outside the main deformation area produced by Siling Co level changes.

In conclusion, we tentatively argue that significant water table changes (a few meters) may only occur around the Lake Siling Co shores, along the low areas located to the east and northeast side of the lake, and within endorheic depressions further away from the lake, mainly on the northwestern side of the lake. With an average porosity of 20%, we conclude that the additional underground water load within the subsidence bowl is not likely to exceed 10 to 20% of the lake load change, and thus cannot explain the observed excessive subsidence rate compared to predictions of the purely elastic model.

6.2. Elastic Moduli and Poroelasticity

Static elastic moduli might be significantly lower than dynamic elastic moduli, as pore fluid pressure is not locally in equilibrium at high frequency [*Thomsen*, 1985]. Extended differential self-consistent models built by *Ravalec and Guéguen* [1996] and *Adelinet et al.* [2010] show that pore pressure effects on bulk and shear moduli depend strongly on the density and aspect ratio of cracks, and less on the density of equant pores. Hence, undrained moduli obtained from V_P/V_S measurements might exceed values of undrained static moduli by ~20% in the shallow part of the crust (first 4 km) where cracks might remain open.

In addition, the strain response to surface load evolves with time toward drained condition. Here two poroelastic effects compete with each other: (1) Compressibility is larger under drained than undrained conditions, resulting in an increased subsidence through time; (2) The increased pore pressure induced by lake level increase should also diffuse away through time and result in a decreased subsidence. The latter uplift effect is observed in residual maps along some part of the lake shores, as in *Cavalié et al.* [2007]. The effect of drained/undrained conditions on the bulk modulus might reach 50% [*Cheng and Johnston*, 1981; *Adelinet et al.*, 2010] for some porous rocks but decreases again strongly with confining pressure.

We have shown in section 4.2.3 that the sensitivity of the observed subsidence to elastic parameters is maximum from depth of 10 km to 20 km, such that a decrease of the bulk modulus by 25% on average in the first 5 km cannot strongly impact the computed subsidence. Furthermore, for poroelastic effects to take place at the scale of the deformation pattern, i.e., approximately 50 km, over a decade, would require unrealistically high-hydraulic diffusivities. Therefore, we conclude that deviations of elastic parameters from V_P/V_S derived values in a poroelastic context cannot explain the amplitude of the observed subsidence.

6.3. Viscosity Structure

In this section we discuss the results of viscoelastic models and their implications for the structure of the lithosphere. Part of the modeling uncertainties are related to the absence of knowledge on the lake level history before 1972. Broad-scale viscous uplift or subsidence could occur in the period 1992 to 2010 due lake level changes before 1972. Using the approximate relaxation timescale obtained for our best fit three-layer model, $\tau \approx 13$ yr, the effect of a load change occurring before 1972 on deformation rates in 1992 to 2005 is small and is approximately 40% lower in 2005 than in 1996. On Figure 10b, we may draw a slight positive trend in the 1992–1999 data, which may represent a small inherited effect from past loads. Continuing this trend to 2011, with a lower rate, would imply an inherited contribution from past loads to the 1999–2011 deformation reaching at most ~15%. Taking into account this hypothetic contribution from past loads would result in a small increase in the best fit viscosity.

A three-layer viscoelastic model with ductile deformation in the crust below 30 km and an effectively elastic mantle is our preferred model to explain the observed temporal evolution of the deformation, with very

good match to both its amplitude and its shape. The data exclude a large contribution from asthenospheric ductile flow on a decade timescale. The deformation amplitude decreases while viscosity or elastic thickness increases, and is proportional to the third power of the ductile layer thickness, which explains the trade-offs in Figure 11. On the other hand, both larger elastic thickness and larger ductile layer thickness imply a larger spatial extent of the deformation. For the two-layer model with a ductile half-space, a small elastic thickness, thus a relatively large viscosity, is necessary to restrict the shape in distance around the lake (Figure 14). However, the fit is not as good as that obtained with the three-layer model. Setting the top of the crustal ductile layer at 15 km depth, produces a deformation pattern too concentrated around the lake shores, if the viscous layer extends only down to the Moho. A better fit is obtained for a viscous half-space below 15 km. We can therefore expect that a viscous layer restricted to the middle crust between, for instance, 15 and 50 km depth would produce a fit to observations worse than when it extends down to the Moho. Hence, we exclude a thin ductile channel located in the middle crust. We conclude that the data favors a low-viscosity layer below 25 to 35 km down to the Moho at 65 km, with a viscosity of $1-3 \times 10^{18}$ Pa s. If thinner, the ductile channel should start deeper in the crust and the viscosity should decrease accordingly.

These estimates of viscosity and elastic thickness can be compared to other results obtained in Tibet for comparable timescales, i.e., mainly using the observations of postseismic motion following earthquakes. However, these studies suffer from interpretation ambiguity between afterslip occurring mainly in the seismogenic layer and deeper viscoelastic relaxation. The 2001 M_w 7.8 Kokoxili earthquake produced first rapid then slower postseismic deformation that has been fitted by viscoelastic relaxation and/or by afterslip located in between coseismic patches [*Ryder et al.*, 2011; *Wen et al.*, 2012]. The authors conclude that InSAR observations cannot in this case distinguish between localized (afterslip) in the middle crust and distributed (viscoelastic relaxation) deformation in the crust with a viscosity of $2-5 \times 10^{19}$ Pa s [*Wen et al.*, 2012]. The postseismic motion following the 1997 M_w 7.6 Manyi (Tibet) earthquake is explained either by afterslip or by viscoelastic relaxation with two timescales (implying a transient or a power law ductile rheology) [*Ryder et al.*, 2007]. Using a depth dependent rheology, the viscosity reaches 2×10^{18} Pa s at the Moho [*Yamasaki and Houseman*, 2012]. The Nima-Gaize, 2008, M_w6.4, normal fault earthquake was followed by shallow afterslip with a small decay time of 1 month. In that case, the surface deformation due to deep viscoelastic motion could not be detected [*Ryder et al.*, 2010]. Finally, our rheological structure agrees well with that derived by [*Huang et al.*, 2014] from far-field postseismic displacement on the Tibet side of the 2008, M_w7.8 Wenchuan earthquake ($H_e = 45$ km, $\eta = 10^{18}$ Pa s).

The elastic thickness obtained here at a decade timescale can be viewed as an upper bound for elastic thickness obtained from Holocene markers, the latter being itself larger than that obtained at geological timescale. The present-day distortion from horizontality of palaeoshorelines can constrain lithospheric flexural rigidity and/or crust viscosity. *England et al.* [2013] showed that the highest stand of some palaeolakes located west of Siling Co remained approximately horizontal, indicating either an elastic flexural support of the load with H_e greater than 20–25 km or a viscous relaxation timescale larger than the loading or unloading timescales (i.e., $\eta > 10^{20}$ Pa s). Our best fit model with a ductile channel below 25 to 35 km agrees with the first explanation. Longer-term elastic support of relief in central Tibet based on gravity anomalies or on flexural bending of rift flanks are lower than 10 km [*Masek et al.*, 1994; *Braitenberg et al.*, 2003]. This low flexural rigidity is thus indicative of a shallow ductile behavior of the crust on a million year timescale.

The importance of a ductile middle to lower crust in the building of thickened crust of Tibet [*Royden et al.*, 1997] and on its state of stress [*Copley et al.*, 2011] has been strongly debated. The rheological structure proposed here in the region of Siling Co Lake in central Tibet should permit significant mass transport in response to pressure (topography) gradient. However, it is important to note that the present-day rheological structure is derived from the response of an already thickened crust. The deformation observed around Siling Co Lake might also be the signature of a transient rheology and not be applicable for steady state flows.

7. Conclusion

The deformation measured by InSAR associated with recent water level changes of the Siling Co Lake allow us to probe the crust and uppermost mantle mechanical properties beneath central Tibet. High temporal sampling of the lake level between 1995 and 2011 is obtained by mixing altimetric information with lake surface measurement on LANDSAT images, reducing the error by averaging independent data. The Siling Co

lake level, after being more or less stagnant for 1973–1999, shows a steep increase at a rate of about 1.0 m/yr until 2006, followed by a slow down until 2011.

All available ERS and Envisat SAR data on two parallel tracks have been processed using a small baseline strategy, forming four independent time series from 1992 to 2011 and from 2003 to 2010, respectively. They display a bowl shape subsidence of amplitude ~5 mm/yr, that is clearly associated with the increased lake load on the lithosphere. The phase delay map time series are adjusted by 3-D layered viscoelastic models of the lithosphere deformation in response to the lake load. The prediction of surface deformation by elastic modeling taking into account reasonably well-constrained elastic parameters (derived from seismic studies) is 2–3 times too low. Best fit models using the same elastic structure but a ductile lower crust reproduce well the observed deformation.

To further discuss the significance of this mean square adjustment, we extract more precisely the temporal evolution of the subsidence signal by correlating the data to a spatial template, defined as the predicted spatial pattern of subsidence for a few best fit models. We show that indeed the amplitude of the surface subsidence signal closely follows the lake level evolution. However, a slight departure from the lake level evolution is observed from 2007 to 2010, where subsidence continues at nearly the same rate while water level stagnates. This behavior is well reproduced by viscoelastic models. Furthermore, we extract the spatial pattern of subsidence by correlating the data to a temporal template, defined as the predicted amplitude evolution for a best fit viscoelastic model. The data shows that the subsidence occurs only up to 90 km from the lake center of mass, a feature well explained in case of ductile flow no deeper than the Moho.

We conclude that the data are best explained by viscoelastic models in which the crust between 25 and 35 km and the Moho has a viscosity of $1-3\times10^{18}$ Pa s, and for which there is no contribution from deeper ductile flow at the observation timescale. This requires the lithospheric mantle and asthenosphere viscosity to be large enough (larger than a few 10^{19} Pa s). These results have been obtained assuming that (1) elastic moduli can be inferred directly from the V_P/V_S structure estimated for the Tibetan lithosphere; (2) the hydrological load is mostly contained in the lake; and (3) no significant poroelastic response to water load occurs. The possible impact of these three simplifications have been discussed qualitatively. Although they cannot be quantified due to the lack of in situ data, we argue that their effect on surface deformation should be small and does not significantly alter the viscosity structure we obtained using viscoelastic models adjustment.

Acknowledgments

The ESA-MOST Dragon 2 Cooperation program sponsored cooperation visits between China and France, master student fellowships, and all SAR data acquisition. The LANDSAT images were made freely available through the GLOVIS USGS website. The modeling code was originally written by L. Fleitout. This work was supported by the EFIDIR project (http://www.efidir.fr) (ANR-07-MDCO-004), by PNTS INSU, by TOSCA CNES, and by the CNRS défi "Mastodons." We thank E. Hetland and one anonymous reviewer for their constructive comments on the manuscript.

References

Adelinet, M., J. Fortin, and Y. Guéguen (2010), Dispersion of elastic moduli in a porous-cracked rock: Theoretical predictions for squirt-flow, *Tectonophysics*, *503*(12), 173–181, doi:10.1016/j.tecto.2010.10.012.

Berardino, P., G. Fornaro, R. Lanari, and E. Sansosti (2002), A new algorithm for surface deformation monitoring based on small baseline differential SAR interferograms, *IEEE Trans. Geosci. Remote Sens.*, *40*, 2375–2383, doi:10.1109/TGRS.2002.803792.

Bills, B. G., D. R. Currey, and G. A. Marshall (1994a), Viscosity estimates for the crust and upper mantle patterns of lacustrine shoreline deformation in the Eastern Great Basin, *J. Geophys. Res.*, *99*, 22,059–22,086, doi:10.1029/94JB01192.

Bills, B. G., S. L. de Silva, D. R. Currey, R. S. Emenger, K. D. Lillquist, A. Donnellan, and B. Worden (1994b), Hydro-isostatic deflection and tectonic tilting in the Central Andes: Initial result of a GPS survey of Lake Minchin shorelines, *Geophys. Res. Lett.*, *21*(4), 293–296, doi:10.1029/93GL03544.

Bills, B. G., K. D. Adams, and S. G. Wesnousky (2007), Viscosity structure of the crust and upper mantle in western Nevada from isostatic rebound patterns of the late Pleistocene Lake Lahontan high shoreline, *J. Geophys. Res.*, *112*, B06405, doi:10.1029/2005JB003941.

Braitenberg, C., Y. Wang, J. Fang, and H. T. Hsu (2003), Spatial variations of flexure parameters over the Tibet-Quinghai Plateau, *Earth. Planet. Sci. Lett.*, *205*(3–4), 211–224, doi:10.1016/S0012-821X(02)01042-7.

Bürgmann, R., and G. Dresen (2008), Rheology of the lower crust and upper mantle: Evidence from rock mechanics, geodesy, and field observations, *Annu. Rev. Earth Planet. Sci.*, *36*, 531–561, doi:10.1146/annurev.earth.36.031207.124326.

Cathles, L. M. (1975), *The Viscosity of the Earth's Mantle*, 386 pp., Princeton Univ. Press, Princeton, N. J.

Cavalié, O., M.-P. Doin, C. Lasserre, and P. Briole (2007), Ground motion measurement in the Lake Mead area, Nevada, by differential synthetic aperture radar interferometry time series analysis: Probing the lithosphere rheological structure, *J. Geophys. Res.*, *112*, B03403, doi:10.1029/2006JB004344.

Cavalié, O., C. Lasserre, M.-P. Doin, G. Peltzer, S. Jianbao, X. Xiwei, and Z.-K. Shen (2008), Measurement of interseismic strain across the Haiyuan fault (Gansu, China), by InSAR, *Earth Planet. Sci. Lett.*, *275*, 246–257, doi:10.1016/j.epsl.2008.07.057.

Chao, B. F., Y. H. Wu, and Y. S. Li (2008), Impact of artificial reservoir water impoundment on global sea level, *Science*, *320*, 212–214, doi:10.1126/science.1154580.

Cheng, C. H., and D. H. Johnston (1981), Dynamic and static moduli, *8*(1), 39–42, doi:10.1029/GL008i001p00039.

Cheng, G., and T. Wu (2007), Responses of permafrost to climate change and their environmental significance, Qinghai-Tibet Plateau, *J. Geophys. Res.*, *112*, F02S03, doi:10.1029/2006JF000631.

Clark, M. K., and L. H. Royden (2000), Topographic ooze: Building the eastern margin of Tibet by lower crustal flow, *Geology*, *28*(8), 703–706, doi:10.1130/0091-7613(2000)28<703:TOBTEM>2.0.CO;2.

Clark, M. K., M. A. House, L. H. Royden, K. X. Whipple, B. C. Burchfiel, X. Zhang, and W. Tang (2005), Late Cenozoic uplift of southeastern Tibet, *Geology*, *33*(6), 525–528, doi:10.1130/G21265.1.

Cohen, S. C. (1998), On the rapid postseismic uplift along Turnagian Arm, Alaska, following the 1964 Prince William Sound earthquake, *Geophys. Res. Lett.*, *25*, 1213–1215, doi:10.1029/98GL00860.
Copley, A., J.-P. Avouac, and B. P. Wernicke (2011), Evidence for mechanical coupling and strong Indian lower crust beneath southern Tibet, *Nature*, *472*, 79–81, doi:10.1038/nature09926.
Dixon, J. E., T. H. Dixon, D. R. Bell, and R. Malservisi (2004), Lateral variation in upper mantle viscosity: Role of water, *Earth Planet. Sci. Lett.*, *222*, 451–467, doi:10.1016/j.epsl.2004.03.022.
Doin, M.-P., F. Lodge, S. Guillaso, R. Jolivet, C. Lasserre, G. Ducret, R. Grandin, E. Pathier, and V. Pinel (2011), Presentation of the small baseline NSBAS processing chain on a case example: The Etna deformation monitoring from 2003 to 2010 using Envisat data. paper ESA SP-697 presented at Fringe 2011 Workshop, Frascati, Itally, 19–23 Sept.
England, P. C., R. Walker, B. Fu, and M. Floyd (2013), A bound on the viscosity of the Tibetan crust from the horizontality of palaeolake shorelines, *Earth. Planet. Sci. Lett.*, *375*, 44–56, doi:10.1016/j.epsl.2013.05.001.
Farr, T. G., and M. Kobrick (2000), Shuttle radar topography mission produces a wealth of data, *Eos Trans. AGU*, *81*(48), 583–585.
Fielding, E. J., and D. McKenzie (2012), Lithospheric flexure in the Sichuan Basin and Longmen Shan at the eastern edge of Tibet, *Geophys. Res. Lett.*, *39*, L09311, doi:10.1029/2012GL051680.
Fleming, K., Z. Martinec, and D. Wolf (2007), Glacial-isostatic adjustment and the viscosity structure underlying the Vatnajiökull Ice Cap, Iceland, *Pure Appl. Geophys.*, *164*(4), 751–768, doi:10.1007/s00024-007-0187-6.
Freed, A. M., R. Bürgmann, E. Calais, J. Freymueller, and S. Hreinsdóttir (2006), Implications of deformation following the 2002 Denali, Alaska, earthquake for postseismic relaxation processes and lithospheric rheology, *J. Geophys. Res.*, *111*, B01401, doi:10.1029/2005JB003894.
Haines, S. S., S. L. Klemperer, L. Brown, J. Guo, J. Mechie, R. Meissner, A. Ross, and W. Zhao (2003), INDEPTH III seismic data: From surface observations to deep crustal processes in Tibet, *Tectonics*, *22*(1), 1001, doi:10.1029/2001TC001305.
Hammond, W. C., C. Kreemer, and G. Blewitt (2009), Geodetic constraints on contemporary deformation in the northern walker lane: 3. Central Nevada seismic belt postseismic relaxation, in *Late Cenozoic Structure and Evolution of the Great Basin Sierra Nevada Transition*, edited by J. S. Oldow and P. H. Cashman, *Geol. Soc. Am. Spec. Pap.*, vol. 447, 33–54, Geol. Soc. Am., Boulder, Colo., doi:10.1130/2009.2447(03).
He, J., and J. Chéry (2008), Slip rates of the Altyn Tagh, Kunlun and Karakorum faults (Tibet) from 3D mechanical modeling, *Earth. Planet. Sci. Lett.*, *274*, 50–58, doi:10.1016/j.epsl.2008.06.049.
Hilley, G. E., K. M. Johnson, M. Wang, Z.-K. Shen, and R. Bürgmann (2009), Earthquake-cycle deformation and fault slip rates in northern Tibet, *Geology*, *37*(1), 31–34, doi:10.1130/G25157A.1.
Huang, M.-H., R. Bürgmann, and A. Freed (2014), Probing the lithospheric rheology across the eastern margin of the Tibetan Plateau, *Earth. Planet. Sci. Lett.*, *396*, 88–96, doi:10.1016/j.epsl.2014.04.003.
Hyndman, R. D., C. A. Currie, and S. P. Mazzotti (2005), Subduction zone backarcs, mobile belts, and orogenic heat, *GSA Today*, *15*, 4–10, doi:10.1130/1052-5173(2005)015<4:SZBMBA>2.0.co;2.
James, T. S., E. J. Gowan, I. Wada, and K. Wang (2009), Viscosity of the asthenosphere from glacial isostatic adjustment and subduction dynamics at the Northern Cascadia subduction zone, British Columbia, Canada, *J. Geophys. Res.*, *114*, B04405, doi:10.1029/2008JB006077.
Jolivet, R., C. Lasserre, M.-P. Doin, S. Guillaso, G. Peltzer, R. Dailu, J. Sun, Z.-K. Shen, and X. Xu (2012), Shallow creep on the Haiyuan Fault (Gansu, China) observed by SAR interferometry, *J. Geophys. Res.*, *117*, B06401, doi:10.1029/2011JB008732.
Kang, S., Y. Xu, Q. You, W.-A. Flugel, N. Pepin, and T. Yao (2010), Review of climate and cryospheric change in the Tibetan Plateau, *Environ. Res. Lett.*, *5*, 015101, doi:10.1088/1748-9326/5/1/015101.
Kaufmann, G., and F. Amelung (2000), Reservoir-induced deformation and continental rheology in the vicinity of Lake Mead, Nevada, *J. Geophys. Res.*, *105*(B7), 16,381–16,358, doi:10.1029/2000JB900079.
Lambeck, K., P. Johnston, C. Smither, and M. Nakada (1996), Glacial rebound of the British Isles-III. Constraints on mantle viscosity, *Geophys. J. Int.*, *125*, 340–354, doi:10.1111/j.1365-246X.1996.tb00003.x.
Lambeck, K., C. Smither, and P. Johnston (1998), Sea-level change, glacial rebound and mantle viscosity for northern Europe, *Geophys. J. Int.*, *134*, 102–144, doi:10.1046/j.1365-246x.1998.00541.x.
Langin, W. R., L. D. Brown, and E. A. Sandvol (2003), Seismicity of Central Tibet from project INDEPTH III seismic recordings, *Bull. Seismol. Soc. Am.*, *93*(5), 2146–2159, doi:10.1785/0120030004.
Larsen, C. F., R. J. Motyka, J. T. Freymueller, K. A. Echelmeyer, and E. R. Ivins (2005), Rapid viscoelastic uplift in southeast Alaska caused by post-little ice age glacial retreat, *Earth Planet. Sci. Lett.*, *237*(3–4), 548–560, doi:10.1016/j.epsl.2005.06.032.
Li, D., Y. Li, B. Ma, G. Dong, L. Wang, and J. Zhao (2009), Lake-level fluctuations since the Last Glaciation in Selin Co (lake), Central Tibet, investigated using optically stimulated luminescence dating of beach ridges, *Environ. Res. Lett.*, *4*, 045204, doi:10.1088/1748-9326/4/4/045204.
Lopez-Quiroz, P., M.-P. Doin, F. Tupin, P. Briole, and J.-M. Nicolas (2009), Time series analysis of Mexico City subsidence constrained by radar interferometry, *J. Appl. Geophys.*, *69*, 1–15, doi:10.1016/j.jappgeo.2009.02.006.
Loveless, J., and B. Meade (2011), Partitioning of localized and diffuse deformation in the Tibetan Plateau from joint inversions of geologic and geodetic observations, *Earth Planet. Sci. Lett.*, *303*(12), 11–24, doi:10.1016/j.epsl.2010.12.014.
Masek, J. G., B. L. Isacks, E. J. Fielding, and J. Browaeys (1994), Rift flank uplift in Tibet: Evidence for a viscous lower crust, *Tectonics*, *13*(3), 659–667, doi:10.1029/94TC00452.
Mechie, J., S. V. Sobolev, L. Ratschbacher, A. Y. Babeyko, G. Bock, A. G. Jones, K. D. Nelson, K. D. Solon, L. D. Brown, and W. Zhao (2004), Precise temperature estimation in the Tibetan crust from seismic detection of the $\alpha - \beta$ quartz transition, *Geology*, *32*, 601–604, doi:10.1130/G20367.1.
Meng, K., X. Shi, E. Wang, and F. Liu (2011), High-altitude salt lake elevation changes and glacial ablation in Central Tibet, 2000–2010, *Chin. Sci. Bull.*, *57*(5), 525–534, doi:10.1007/s11434-011-4849-5.
Mügler, I., et al. (2009), A multi-proxy approach to reconstruct hydrological changes and Holocene climate development of Nam Co, Central Tibet, *J. Paleolimnol.*, *43*(4), 625–648, doi:10.1007/s10933-009-9357-0.
Nakiboglu, S. M., and K. Lambeck (1983), A reevaluation of the isostatic rebound of Lake Bonneville, *J. Geophys. Res.*, *88*(B12), 10,439–10,447, doi:10.1029/JB088iB12p10439.
Nof, R. N., A. Ziv, M.-P. Doin, G. Baer, Y. Fialko, S. Wdowinski, Y. Eya, and Y. Bock (2012), Rising of the lowest place on earth due to dead sea water-level drop: Evidence from SAR interferometry and GPS, *J. Geophys. Res.*, *117*, B05412, doi:10.1029/2011JB008961.
Peltier, W. R., and X. Jiang (1996), Glacial isostatic adjustment and Earth rotation: Refined constraints on the viscosity of the deepest mantle, *J. Geophys. Res.*, *101*, 3269–3290, doi:10.1029/95JB01963.
Peltzer, G., P. Rosen, F. Rogez, and K. Hudnut (1998), Poroelastic rebound along the Landers 1992 earthquake surface rupture, *J. Geophys. Res.*, *103*(B12), 30,131–30,145, doi:10.1029/98JB02302.

Piersanti, A. (1999), Postseismic deformation in Chile: Constraints on the asthenospheric viscosity, *Geophys. Res. Lett.*, *26*, 3157–3160, doi:10.1029/1999GL005375.
Pollitz, F., G. Peltzer, and R. Burgmann (2000), Mobility of continental mantle: Evidence from postseismic geodetic observations following the 1992 Landers earthquake, *J. Geophys. Res.*, *105*(B4), 8035–8054.
Ravalec, M. L., and Y. Guéguen (1996), High- and low-frequency elastic moduli for a saturated porous/cracked rock differential self-consistent and poroelastic theories, *Geophysics*, *61*, 1080–1094.
Rosen, P. A., S. Hensley, G. Peltzer, and M. Simons (2004), Updated repeat orbit interferometry package released, *Eos Trans. AGU*, *85*(5), 47.
Royden, L. H., B. C. Burchfiel, R. W. King, E. Wang, Z. Chen, F. Shen, and Y. Liu (1997), Surface deformation and lower crustal flow in eastern Tibet, *Science*, *276*(5313), 788–790, doi:10.1126/science.276.5313.788.
Ryder, I., T. W. B. Parsons, and G. Funning (2007), Post-seismic motion following the 1997 Manyi (Tibet) earthquake: InSAR observations and modeling, *Geophys. J. Int.*, *169*, 1009–1027, doi:10.1111/j.1365-246X.2006.03312.x.
Ryder, I., R. Bürgmann, and J. Sun (2010), Tandem afterslip on connected fault planes following the 2008 Nima-Gaize (Tibet) earthquake, *J. Geophys. Res.*, *115*, B03404, doi:10.1029/2009JB006423.
Ryder, I., R. Bürgmann, and F. Pollitz (2011), Low crustal relaxation beneath the Tibetan Plateau and Qaidam Basin following the 2001 Kokoxili earthquake, *Geophys. J. Int.*, *187*, 613–630, doi:10.1111/j.1365-246X.2011.05179.x.
Satirapod, C., I. Trisirisatayawong, L. Fleitout, J. Garaud, and W. Simons (2013), Vertical motions in Thailand after the 2004 Sumatra-Andaman Earthquake from GPS observations and its geophysical modelling, *Adv. Space Res.*, *51*, 1565–1571, doi:10.1016/j.asr.2012.04.030.
Taylor, M., and G. Peltzer (2006), Current slip rates on conjugate strike-slip faults in central Tibet using synthetic aperture radar interferometry, *J. Geophys. Res.*, *1113*, B12402, doi:10.1029/2005JB004014.
Taylor, M., and A. Yin (2009), Active structures on the Tibetan Plateau and surrounding regions: Relationships with earthquakes, contemporary strain, and late Cenozoic volcanism, *Geosphere*, *5*, 199–214, doi:10.1130/GES00217.1.
Thomsen, L. (1985), Biot-consistent elastic moduli of porous rocks: Low frequency limit, *Geophysics*, *50*, 2797–2807, doi:10.1190/1.1441900.
Trubienko, O., L. Fleitout, J.-D. Garaud, and C. Vigny (2013), Interpretation of interseismic deformations and the seismic cycle associated with large subduction earthquakes, *Tectonophysics*, *589*, 126–141, doi:10.1016/j.tecto.2012.12.027.
Wang, B., Q. Bao, B. Hoskins, G. Wu, and Y. Liu (2008), Tibetan Plateau warming and precipitation changes in East Asia, *Geophys. Res. Lett.*, *35*, L14702, doi:10.1029/2008GL03433.
Wen, Y., Z. Li, C. Xu, I. Ryder, and R. Bürgmann (2012), Postseismic motion after the 2001 MW 7.8 Kokoxili earthquake in Tibet observed by InSAR time series, *J. Geophys. Res.*, *117*, B08405, doi:10.1029/2011JB009043.
Wu, Y., and L. Zhu (2008), The response of lake-glacier variations to climate change in Nam Co Catchment, central Tibetan Plateau, during 1970–2000, *J. Geog. Sci.*, *18*, 177–189, doi:10.1007/s11442-008-0177-3.
Xie, J., R. Gok, J. Ni, and Y. Aoki (2004), Lateral variations of crustal seismic attenuation along the INDEPTH profiles in Tibet from *LgQ* inversion, *J. Geophys. Res.*, *109*, B10308, doi:10.1029/2004JB002988.
Xu, Z. X., T. L. Gong, and J. Y. Li (2008), Decadal trend of climate in the Tibetan Plateau-regional temperature and precipitation, *Hydrol. Processes*, *22*, 3056–3065, doi:10.1002/hyp.6892.
Yamasaki, T., and G. A. Houseman (2012), The crustal viscosity gradient measured from post-seismic deformation: A case study of the 1997 Manyi (Tibet) earthquake, *Earth. Planet. Sci. Lett.*, *351–352*, 105–114, doi:10.1016/j.epsl.2012.07.030.
Yao, T., J. Pu, A. Lu, Y. Wang, and W. Yu (2007), Recent glacial retreat and its impact on hydrological processes on the Tibetan Plateau, China, and surrounding regions, *Arct. Antarct. Alp. Res.*, *39*, 642–650, doi:10.1657/1523-0430(07-510).
Zhang, G., H. Xie, S. Kang, D. Yi, and S. F. Ackley (2011), Monitoring lake level changes on the Tibetan Plateau using IceSAT altimetry data (2003–2009), *Remote Sens. Environ.*, *115*(7), 1733–1742, doi:10.1016/j.rse.2011.03.005.
Zhang, Z., and S. L. L. Klemperer (2005), West-east variation in crustal thickness in northern Lhasa Block, central Tibet, from deep seismic sounding data, *J. Geophys. Res.*, *110*, B09403, doi:10.1029/2004JB003139.
Zhao, W., et al. (2001), Crustal structure of central Tibet as derived from project INDEPTH wide-angle seismic data, *Geophys. J. Int.*, *145*, 486–498, doi:10.1046/j.0956-540x.2001.01402.x.